UNIVERSIDAD DE CONCEPCIÓN
FACULTAD DE CIENCIAS FÍSICAS Y MATEMÁTICAS

DEEP KILOPARSEC VIEW OF THE MOLECULAR GAS IN A MASSIVE STAR-FORMING GALAXY AT COSMIC NOON

Una vista profunda en kiloparsecs del gas molecular en una galaxia formadora de estrellas masiva del mediodía cósmico

By: Sebastián Arriagada Neira

Thesis presented to the Faculty of Physical Sciences and Mathematics of the University of Concepción to obtain the degree of Master in Astronomy

September 2024
Concepción, Chile

Advisor: Rodrigo Herrera-Camus

A mis seres queridos

AGRADECIMIENTOS

En primer lugar, me gustaría expresar mi más profundo y sincero agradecimiento a mis padres. Su apoyo incondicional, inclusive en los momentos en los que dudaba de si había elegido el camino correcto, fue fundamental para que pudiera alcanzar este logro. Les estaré eternamente agradecido por todos los sacrificios que han debido hacer a lo largo de los años, permitiéndome llegar hasta donde estoy ahora.

Me gustaría agradecer al Dr. Rodrigo Herrera-Camus, mi asesor de tesis, por brindarme la oportunidad de trabajar en un proyecto de tanto valor. Su confianza en mi, paciencia y orientación fueron pilares fundamentales a lo largo de todo este proceso. Atesoraré cada uno de los consejos que me ha dado durante estos años y espero, en un futuro, poder convertirme en un investigador que esté a la altura de las expectativas que ha depositado en mí. Agradezco igualmente al Dr. Vicente Villanueva por su gran ayuda en la etapa final de este trabajo y por sus consejos, tanto en lo personal como lo profesional, que han servido de guía para mi futuro.

Finalmente, me gustaría agradecer a cada una de las personas que me han acompañado en este camino. En especial, agradezco a Omar B., María José C., Isabel I., Valentina I., Melissa F., Pedro G., Sebastián G., Macarena S. y Jorge S., quienes conocí en los primeros años de carrera y cuyas amistades valoro inmensamente. Agradezco igualmente a Felipe A. y Andrés T., quienes me han acompañado desde mi etapa en el colegio. Nuestras caminatas por la playa han sido de gran ayuda, tanto para desconectar de la ciencia como para superar momentos difíciles, especialmente durante el tiempo en pandemia.

Resumen

Presentamos observaciones profundas ($\sim$20 hr) y de alta resolución angular del Atacama Large Millimeter/submillimeter Array (ALMA) de las transiciones CO $(4-3)$ y [CI] $(1-0)$, junto con el continuo de polvo a 630 μm en BX610 –una galaxia masiva de secuencia principal en la época de máxima formación estelar cósmica ($z = 2.21$). Combinadas con observaciones profundas SINFONI del Very Large Telescope (VLT) de la línea Hα, estas observaciones permiten una caracterización detallada del gas molecular y de la actividad de formación estelar en escalas de kiloparsecs. Nuestro análisis revela que la excitación del gas molecular, trazada por la razón de luminosidad de línea $L'_{\mathrm{CO}\ (4-3)}\ /\ L'_{\mathrm{[CI]}\ (1-0)}$, disminuye al aumentar el radio galactocéntrico. Mientras que las razones de luminosidad de línea en la periferia son similares a las que suelen encontrarse en galaxias de secuencia principal a $z \sim 1$, las razones en las regiones centrales de BX610 son comparables a las observadas en starbursts locales. En el suroeste de BX610 también hay un clump gigante de formación estelar extra-nuclear que muestra una elevada actividad de formación estelar, abundancia de gas molecular y excitación de gas molecular. Además, la región central de BX610 es rica en gas molecular ($M_{\mathrm{mol}}/M_\star \approx 1$), pero con el alto nivel actual de actividad de formación estelar, el gas molecular se agotará en $\sim$450 Myr. Esto, junto con la evidencia de un rápido inflow de gas molecular hacia el centro (Genzel et al., 2023), sugiere que BX610 puede estar experimentando una fase evolutiva a menudo denominada compactación húmeda, que se espera que conduzca al agotamiento del gas central y a la subsiguiente extinción de la actividad de formación estelar.

Keywords – galaxias: evolución – galaxias: alto redshift – galaxias: ISM – galaxias: gas molecular – estrellas: formación

Abstract

We present deep ($\sim$20 hr), high-angular resolution Atacama Large Millimeter/submillimeter Array (ALMA) observations of the CO $(4-3)$ and [CI] $(1-0)$ transitions, along with the rest-frame 630 μm dust continuum, in BX610—a massive, main-sequence galaxy at the peak epoch of cosmic star formation ($z = 2.21$). Combined with deep Very Large Telescope (VLT) SINFONI observations of the Hα line, these observations enable a detailed characterization of the molecular gas and star formation activity on kiloparsec scales. Our analysis reveals that the excitation of the molecular gas, as traced by the $L'_{\mathrm{CO}\ (4-3)} \,/\, L'_{[\mathrm{CI}]\ (1-0)}$ line luminosity ratio, decreases with increasing galactocentric radius. While the line luminosity ratios in the outskirts are similar to those typically found in main-sequence galaxies at $z \sim 1$, the ratios in the central regions of BX610 are comparable to those observed in local starbursts. There is also a giant extra-nuclear star-forming clump in the southwest of BX610 that exhibits high star formation activity, molecular gas abundance, and molecular gas excitation. Furthermore, the central region of BX610 is rich in molecular gas ($M_{\mathrm{mol}}/M_{\star} \approx 1$), but at the current high level of star formation activity, the molecular gas will be exhausted in $\sim$450 Myr. This, along with evidence for rapid molecular gas inflow toward the center (Genzel et al., 2023), suggests that BX610 may be experiencing an evolutionary phase often referred to as wet compaction, which is expected to lead to central gas depletion and subsequent inside-out quenching of star formation activity.

Keywords – galaxies: evolution – galaxies: high-redshift – galaxies: ISM – galaxies: molecular gas – stars: formation

Contents

List of Tables

List of Figures

Chapter 1

Introduction

1.1 Context

Galaxies are complex systems made up of stars, gas, dust, dark matter, and a supermassive black hole in their center, all of which collectively interact to shape their formation and evolution over cosmic time. The interstellar medium (ISM), consisting of the gas and dust that fill the space between stars, plays a crucial role in this process. The gas, composed mainly of hydrogen and helium, provides the raw material for the formation of new stars. When stars reach the end of their life cycle, they release the heavier elements formed in their cores into the ISM and the circumgalactic medium (CGM). Most of the material in the CGM, along with pristine gas from the intergalactic medium (IGM), is eventually pulled back into the galaxy, fueling future star formation. This collection of physical processes that sustain the gas reservoirs for further star formation is known as the "baryon cycle".

In that sense, understanding the properties of the gas and its connection to ongoing star formation is critical for comprehending how galaxies grow and evolve over cosmic time. However, due to the large timescales involved in these processes, they cannot be observed directly. Instead, astronomers study galaxy populations at different epochs to subsequently draw a complete picture of the evolutionary processes that shape galaxies over time and lead to their current states.

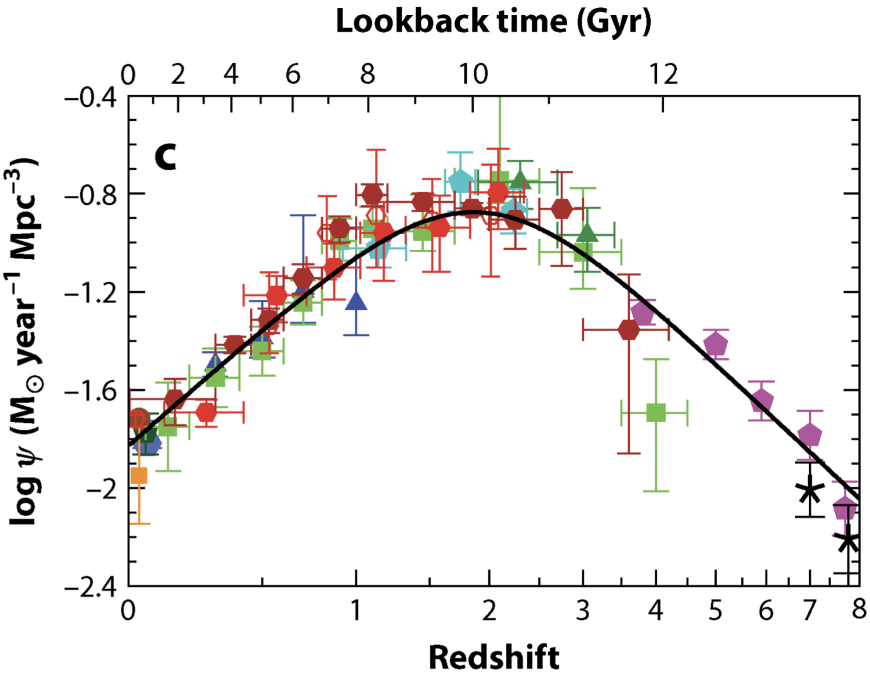

Figure 1.1.1: The cosmic star formation rate density (CSFRD) as a function of redshift. The data points indicate observations from surveys at different wavelengths, while the black line is the best fit. The star formation rate peaks around $z \sim 2$, about 10 billion years ago, and then decreases steadily until the present day. Figure taken from Madau and Dickinson (2014).

1.1.1 The main sequence of star-forming galaxies

Over the past two decades, the number of surveys of individual galaxies at different cosmic epochs has been increasing, revealing the existence of a tight correlation between their integrated star formation rates (SFRs) and their stellar masses ($M_\star$) (e.g., Brinchmann et al., 2004; Daddi et al., 2007; Elbaz et al., 2007, 2011; Noeske et al., 2007).

This relation, known as the "main sequence of star-forming galaxies", includes most of the star-forming galaxies at all redshifts. Above the main sequence, "starburst galaxies" are located, which exhibit SFRs several orders of magnitude higher than expected for their stellar mass. In contrast, "quiescent galaxies", situated below the main sequence, are characterized by high stellar mass, old stellar populations, and minimal star formation.

1.1.2 The cosmic noon

These studies have also traced the evolution of the cosmic star formation rate density (CSFRD) over time (e.g., Lilly et al., 1996; Madau et al., 1996; Hopkins and Beacom, 2006; Madau and Dickinson, 2014). As shown in Figure 1.1.1, CSFRD increased steadily from the earliest epochs until it reached its peak at redshift $z = 1 - 3$, around 10 billion years ago. This period, known as the cosmic noon, denotes the period when most of the stars in the Universe were formed, with about 90% of the total SFR taking place in normal main-sequence galaxies (Rodighiero et al., 2011, 2015). Finally, galaxies underwent a decrease in star formation activity by a factor of 10 up to the present time.

Therefore, the cosmic noon is a crucial time in the study of galaxy evolution, providing insight into the growth of galaxies and the eventual extinction of their star-forming activity. Hence, in main-sequence galaxies, which dominate the epoch, the SFR appears to be well-constrained. However, to fully understand the physical mechanisms driving star formation, it is critical to accurately determine the molecular gas content.

1.2 The Molecular Gas

In galaxies such as the Milky Way, star formation mainly occurs inside giant molecular clouds (GMCs), whose temperature ($T = 10 - 50$ K) and density ($n_{\rm H} \geq 10^3$ cm^{-3}) conditions allow the gas to fragment into clumps where stars are eventually born. In these environments, the dominant component of the molecular gas is the cold molecular hydrogen (H_2). However, since cold H_2 does not have a permanent dipole moment, its lower rotational transitions are forbidden and have upper-level energies of $E/k \sim 500$ K and $E/k \sim 1000$ K that are not reached in GMCs, which makes the H_2 practically undetectable for our purposes (Bolatto et al., 2013). Fortunately, other elements inside GMCs can be used to detect the molecular gas and consequently estimate the total molecular gas content (see Carilli and Walter, 2013, for a review).

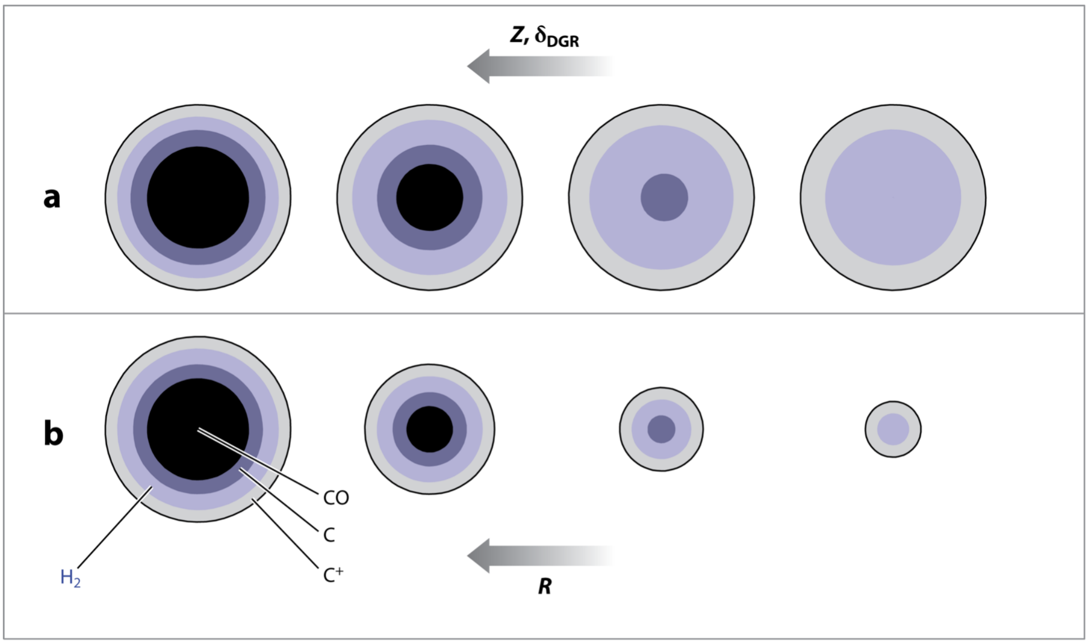

Figure 1.2.1: Illustration of the effects of metallicity on CO and H_2 in a molecular cloud immersed in a uniform radiation field. Panel a shows the scenario with constant cloud size, evidencing that the CO content progressively decreases and eventually disappears as the metallicity decreases. Panel b shows the scenario with constant metallicity. Figure taken from Bolatto et al. (2013).

1.2.1 Molecular gas tracers

1.2.1.1 Carbon monoxide

Carbon monoxide ($^{12}C^{16}O$, hereafter CO), and particularly its first excited state CO $J = 1 \rightarrow 0$ (hereafter CO $(1-0)$) at $\nu_{\rm rest} = 115$ GHz, has traditionally been used to trace the molecular gas content. This preference is due to several key factors: CO is the second most abundant molecule in the ISM after H_2; it has relatively low excitation requirements, with the CO $(1-0)$ rotational transition having an excitation temperature of ~ 5 K; and its low-J emission lines are easily observable through a transparent atmospheric window (at $z = 0$) from ground-based telescopes operating at radio, millimeter and submillimeter frequencies.

In order to estimate the mass of the molecular gas from the emitted CO line luminosity, it is necessary to apply a mass-to-light conversion factor known as the $\alpha_{\rm CO}$ conversion factor. In the Milky Way, the $\alpha_{\rm CO}$ value has been well-calibrated through several independent methods, including gamma-ray emission studies, dust and CO isotopologue observations, and application of the virial theorem (see Bolatto et al., 2013, for a review). However, the $\alpha_{\rm CO}$ value depends strongly on the ISM conditions, such as temperature, density, and metallicity (e.g., Narayanan et al., 2012), so the choice of this value for other galaxies remains a significant source of uncertainty in estimating the actual molecular gas content.

The situation is even more challenging at high redshift (e.g., Carilli and Walter, 2013). In metal-poor environments, as observed in some high-z sources, CO is strongly photodissociated by far-ultraviolet (FUV) photons, while the H_2 content remains mostly intact (see Figure 1.2.1). As a result, using a Milky Way-like $\alpha_{\rm CO}$ conversion factor may lead to an underestimate of the molecular gas mass. Furthermore, at high redshifts, the low-J CO lines are redshifted to frequencies that current observational facilities often cannot access. Hence, it is necessary to use mid- and high-J CO lines, which trace a more excited gas compared to the gas traced with the ground-state transition (for example, the CO $(4-3)$ rotational transition at $\nu_{\rm rest} = 461$ GHz has an excitation temperature of ~ 55 K). To address this issue, an excitation correction factor must be applied to convert the observed CO rotational transition to the ground-state transition, for which $\alpha_{\rm CO}$ is calibrated. However, the value of the excitation correction factor is often obtained from previous studies in other sources, which may introduce additional uncertainty in the calculation of molecular gas content. Therefore, all these challenges highlight the need for alternative methods to estimate the molecular gas content reliably.

1.2.1.2 Atomic carbon

An alternative tracer for the cold molecular gas mass is the atomic carbon ([CI]) emission. Recent studies have tested whether the lower fine structure line of atomic carbon [CI] ($^3P_1 \rightarrow {}^3P_0$) (hereafter [CI] $(1-0)$) at $\nu_{\rm rest} = 492$ GHz could be used as a robust tracer of cold molecular gas (e.g., Papadopoulos et al., 2004; Alaghband-Zadeh et al., 2013; Bothwell et al., 2017; Boogaard et al., 2021; Michiyama et al., 2021; Henríquez-Brocal et al., 2022). Initially, early one-dimensional models suggested that [CI] emission originated from a narrow gas layer located between CO and [CII] in molecular clouds (e.g., Tielens and Hollenbach, 1985), which led to skepticism about the usefulness of the [CI] $(1-0)$ transition as a reliable molecular gas tracer. However, modern theoretical (e.g., Offner et al., 2014; Glover et al.,

2015) and observational (e.g., Ikeda et al., 2002; Kulesa et al., 2005; Requena-Torres et al., 2016; Okada et al., 2019) studies have shown that [CI] emission is indeed associated with CO emission regardless of the environment, supporting its potential as a robust tracer of the bulk molecular gas mass (Papadopoulos et al., 2004; Walter et al., 2011; Henríquez-Brocal et al., 2022). Notably, [CI] emission can persist even in metal-poor and high cosmic-ray environments where CO is significantly photodissociated (e.g., Papadopoulos et al., 2004; Bisbas et al., 2015, 2017; Glover and Clark, 2016). Furthermore, [CI] has certain advantages when studying high-z sources: the [CI] $(1-0)$ emission line is brighter than CO $(1-0)$, making it easier to detect; it is also optically thin (e.g., Ikeda et al., 2002; Shimajiri et al., 2013), allowing it to probe high column density environments; and its excitation temperature of ~ 24 K is low enough to trace the bulk of the cold molecular gas content, unlike the mid- and high-J CO lines, which trace a more excited gas.

Over the past decade, observations of [CI] have extended beyond bright quasars and submillimeter galaxies (e.g., Boogaard et al., 2021; Lee et al., 2021; Henríquez-Brocal et al., 2022). Notably, Valentino et al. (2018, 2020) found a strong correlation between [CI] and CO that is consistent across different redshifts (up to $z \lesssim 3$) and galaxy types, and concluded that [CI] is a reliable tracer of molecular gas, similar to low-J CO lines and dust. However, its application in further studies is limited by the lack of systematic calibration of a [CI]-to-H_2 conversion factor.

1.2.2 Current studies

At the present time, the new generation of mm/sub-mm facilities, including the Atacama Large Millimeter/submillimeter Array (ALMA), the NOrthern Extended Millimeter Array (NOEMA), and the Karl G. Jansky Very Large Array (JVLA), has provided the advanced capabilities necessary to perform both large-scale surveys (e.g., Genzel et al., 2010; Tacconi et al., 2013; Daddi et al., 2010; Valentino et al., 2018, 2020) and detailed studies (e.g., Hodge et al., 2015; Chen et al., 2017; Spilker et al., 2019; Rizzo et al., 2023) of the molecular gas properties in star-forming galaxies at high redshift.

Deep, blind galaxy surveys have recently studied the evolution of molecular gas content in galaxies over cosmic time (e.g., Tacconi et al., 2018; Walter et al., 2020; Tacconi et al., 2020). These studies reveal that the mass of molecular gas slowly

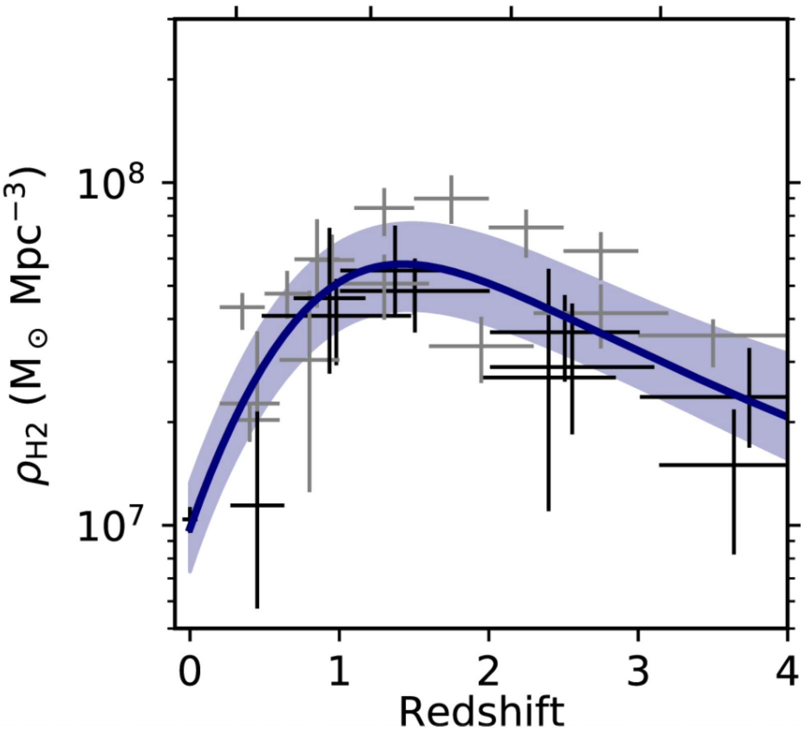

Figure 1.2.2: Cosmic molecular gas mass density as a function of redshift. The data points indicate observations from CO (black points) and dust continuum (gray points) surveys, while the blue line is the best fit. The molecular gas mass density peaks around $z \sim 1 - 3$, which is similar to the trend observed for the CSFRD. The similarity in the cosmic evolution of both quantities suggests that molecular gas is the main driver of the elevated star formation activity observed at the cosmic noon epoch. Figure taken from Walter et al. (2020).

increased from early cosmic epochs, peaked around $z \sim 1 - 3$, and then steadily decreased to the present day (see Figure 1.2.2). This trend, similar to the evolution of the CSFRD (see Figure 1.1.1), suggests that the significant reservoirs of H_2 were the primary drivers of the increased star formation activity during the cosmic noon epoch. In particular, main-sequence galaxies display a high molecular gas fraction ($\mu_{\rm mol} \gtrsim 0.8$) at $z \sim 2 - 3$ (see Figure 1.2.3), highlighting the importance of detailed studies on the molecular gas properties in this galaxy type. However, despite significant progress made in bright submillimeter galaxies (SMGs; e.g., Hodge et al., 2015; Chen et al., 2017), cluster galaxies (e.g., Ikeda et al., 2022), gravitationally lensed dusty galaxies (e.g., Spilker et al., 2015), and compact star-forming galaxies (e.g., Spilker et al., 2019), the molecular gas properties of more typical star-forming galaxies at cosmic noon on ∼kiloparsec scales remain relatively understudied.

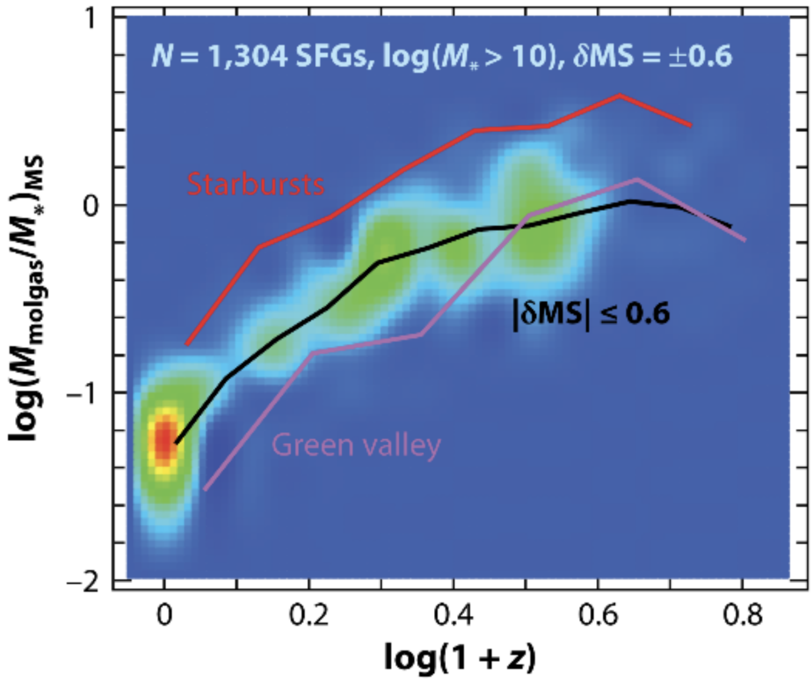

Figure 1.2.3: The molecular gas fraction, $\mu_{\rm mol} = M_{\rm mol}/M_\star$, as a function of redshift. The smoothed distribution of main-sequence galaxies is shown underlying in color. At the same time, the black, red, and purple lines are the binned averages of main-sequence galaxies, starbursts, and galaxies below the main sequence, respectively. Main-sequence galaxies at $z \sim 2$ exhibit, on average, a value of $\mu_{\rm mol} \approx 0.75$. Figure taken from Tacconi et al. (2020).

One area where progress has been made is in understanding the spatially resolved Kennicutt-Schmidt (KS) relation (Kennicutt, 1998) between total molecular gas and SFR. Studies, for example, by Genzel et al. (2013) and Freundlich et al. (2013) have demonstrated that both the slope of the KS relation and the molecular gas depletion timescale ($t_{\rm dep} = M_{\rm mol}/{\rm SFR}$) in galaxies at cosmic noon are broadly consistent with those observed in the local Universe (e.g., Bolatto et al., 2017; Sun et al., 2023)

1.3 This Project

Motivated by the need to characterize the molecular gas properties on ∼kiloparsec scales in a galaxy representative of the cosmic noon, we present in this research the deepest observation to date by ALMA of a typical main-sequence galaxy at $z \sim 2$. The focus of our study, Q2343-BX610 (hereafter BX610), is a main-sequence star-forming galaxy at $z = 2.2103$ with a stellar mass of $M_\star \approx 1.5 \times 10^{11}$ $M_\odot$

(Tacchella et al., 2015) and a SFR ranging from 60 to 200 $M_\odot$ yr^{-1}, depending on the tracer or the level of dust obscuration assumed (Förster Schreiber et al., 2009, 2014; Brisbin et al., 2019). BX610 has been extensively studied across various wavelengths, including optical/near-infrared (Förster Schreiber et al., 2009, 2011a,b, 2014, 2018) and far-infrared (Tacconi et al., 2013; Aravena et al., 2014; Bolatto et al., 2015; Brisbin et al., 2019). Hα observations characterize BX610 as a rotating disk with a massive star-forming clump and no evidence of a nearby companion (Förster Schreiber et al., 2011b, 2018). The galaxy rest-frame optical morphology reveals bar- and spiral-like features (Förster Schreiber et al., 2011a). Additionally, observational evidence suggests that BX610 may host an active galactic nucleus (AGN), but it appears to be relatively weak (Förster Schreiber et al., 2014; Newman et al., 2014).

Previous observational efforts to investigate the physical conditions of the molecular gas in BX610 include JVLA CO $(1-0)$ observations by Bolatto et al. 2015 and IRAM Plateau De Bure Interferometer (PdBI) CO $(4-3,\ 7-6)$ and [CI] $(1-0,\ 2-1)$ observations by Brisbin et al. 2019. However, due to depth and/or angular resolution limitations, these studies have provided only a broad overview of BX610 molecular gas properties. In this context, the new deep ($\sim$20 hr of ALMA time), $\sim$kiloparsec scale ALMA observations presented in this work represent a significant improvement in depth and spatial resolution. The kinematic properties of BX610 based on this dataset have already been analyzed by Genzel et al. (2023), who found that the velocity field of BX610 traced by the CO $(4-3)$ emission line reveals a well-defined rotating disk, with evidence for a rapid inflow of gas towards the central region. The velocity of the radial gas motion is $\sim$95 km s^{-1}, approximately one-third of the rotational velocity.

The research is organized as follows. In Chapter 2, we present the new ALMA observations and the further data reduction, as well as the archive observations used in this work. In Chapter 3, we explain the methods applied to analyze the data and the equations used to derive the physical quantities. In Chapter 4, we present our results and discussion, and finally, in Chapter 5, we summarize the main conclusions. Throughout this research, we assume a Chabrier initial mass function (IMF; Chabrier 2003) and a ΛCDM cosmology with $H_0 = 70$ km s^{-1} Mpc^{-1}, $\Omega_M = 0.3$, and $\Omega_\Lambda = 0.7$. For this cosmology, $1''$ corresponds to 8.259 kpc at $z = 2.2103$.

Chapter 2

Data Products

To analyze the physical conditions of the ISM in BX610, we use ALMA observations along with archival data from the Very Large Telescope (VLT) and Hubble Space Telescope (HST). The key features of these datasets are summarized in the following subsections. The observed and derived properties of BX610 are shown in Table 2.0.1.

2.1 ALMA

ALMA Band 4 observations of BX610 were carried out in July 2021 as part of Cycle 7 (Project ID: 2019.1.01362.S, PI: R. Herrera-Camus). The details of the data calibration and reduction were presented in Genzel et al. (2023) and Lee et al. (2024). In summary, we centered two spectral windows (SPWs) set in the Frequency-Division Mode to detect the redshifted CO $(4-3)$ and [CI] $(1-0)$ transitions with channel widths of 3.906 MHz, and the two remaining SPWs were set in the Time-Division Mode to detect the rest-frame 630 μm dust continuum. The quasar J2253+1608 was used as the flux and bandpass calibrator, and the quasar J2350+1106 was used as the phase calibrator. The ALMA array configurations were chosen to achieve a physical resolution comparable to the Toomre length at this redshift. This resulted in observations with projected baselines of 15 m - 3.7 km that produced an angular resolution of $\approx 0.2''$, which at the redshift of BX610 corresponds to $\approx$1.6 kpc. We integrated for a total of 13.6 hr, which resulted in a total observing time of $\sim$20 hr when including the overheads.

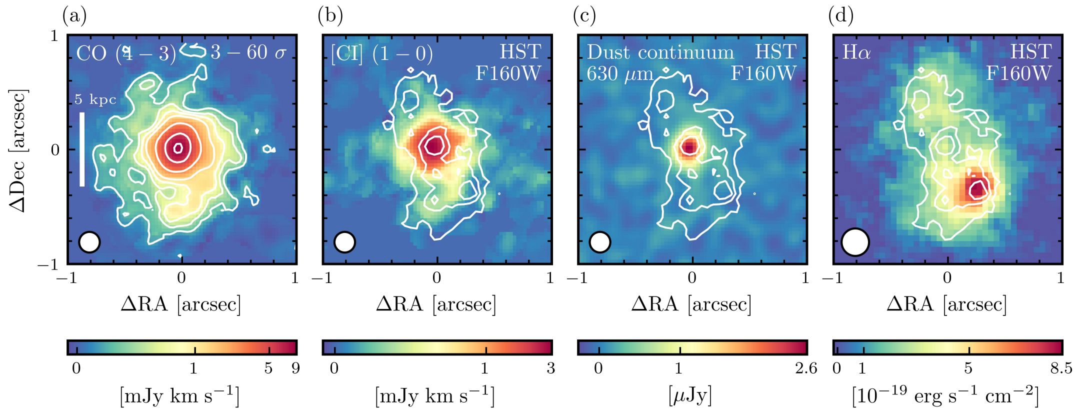

Figure 2.0.1: Multi-wavelength imaging of BX610. (a) CO $(4-3)$ integrated intensity map. The overlaid white contours correspond to the 3, 5, 7, 10, 20, 40, and 60σ levels. The filled circle at the bottom left corner indicates the ALMA-synthesized beam ($\theta = 0.18'' \times 0.18''$). (b) [CI] $(1-0)$ integrated intensity map. The overlaid white contours represent the rest-frame optical emission observed by HST WFC3 F160W. (c) Rest-frame 630 μm dust continuum emission. (d) Hα integrated intensity map. The filled circle at the bottom left corner indicates the SINFONI Hα point-spread function.

Table 2.0.1: Observed and derived properties of BX610.

Parameter	Unit	Value	Reference
RA	hh:mm:ss.ss	23:46:09.43	Erb et al. (2006)
Dec	dd:mm:ss.ss	12:49:19.21	Erb et al. (2006)
Redshift		2.2103	Förster Schreiber et al. (2009)
$R_{\mathrm{eff},\star}$	kpc	4.44 ± 0.08	Förster Schreiber et al. (2011a)
CO $(1-0)$	Jy km s^{-1}	0.105 ± 0.015	Bolatto et al. (2015)
FWHM	km s^{-1}	294 ± 49	Bolatto et al. (2015)
CO $(4-3)$	Jy km s^{-1}	1.55 ± 0.03	This work
FWHM	km s^{-1}	280 ± 12	This work
[CI] $(1-0)$	Jy km s^{-1}	0.54 ± 0.04	This work
FWHM	km s^{-1}	296 ± 32	This work
$S_{630\ \mu\mathrm{m}}$	mJy	0.18 ± 0.01	This work
$M_\star$	10^{11} M$_\odot$	1.55	Tacchella et al. (2015)
SFR	M$_\odot$ yr^{-1}	141 ± 6	Brisbin et al. (2019)
M_{mol}(CO)	10^{11} M$_\odot$	1.2 ± 0.2	This work
M_{mol}([CI])	10^{11} M$_\odot$	1.3 ± 0.1	This work

The data were processed using the Common Astronomy Software Applications package (`CASA`; McMullin et al., 2007) version 6.1.1.15. For visibility calibration, we used the pipeline script provided by the ALMA Regional Center staff. Continuum and cube images were produced by the `TCLEAN` task and deconvolved down to 2σ noise level, initially measured from the dirty map. We finally produced CO $(4-3)$ and [CI] $(1-0)$ line cubes and a 630 μm dust continuum map with a matched, circular beam of $0.18'' \times 0.18''$ using Briggs weighting.

To obtain the CO $(4-3)$ and [CI] $(1-0)$ integrated intensity maps, we used the PYTHON package `BETTERMOMENTS`[1] (Teague and Foreman-Mackey, 2018), applying a mask based on a 2σ clipping of the $2 \times$ FWHM convolved spatial data. The resulting integrated intensity maps of the CO $(4-3)$ and [CI] $(1-0)$ transitions and the dust continuum are shown in Figure 2.0.1. Using the 2D-Gaussian fitting task `IMFIT`, the integrated flux of the dust continuum emission was found to be 0.18 ± 0.01 mJy. As Lee et al. (2024) pointed out, this value is a factor of ~ 2 lower than the flux reported by Brisbin et al. (2019).

2.2 VLT

We include in our study VLT/SINFONI Adaptive Optics (AO)-assisted Hα observations from the SINS/zC-SINF survey (e.g., Förster Schreiber et al., 2009, 2014, 2018). We refer to Förster Schreiber et al. (2018) for a detailed description of the observation and further data reduction. In summary, the galaxy was observed in the K-band for an on-source time of 8.3 hr in LGS-SE AO mode. The achieved angular resolution was $0.24''$ (a physical resolution of ≈ 2 kpc). To obtain the Hα flux map, we followed the line fitting described in Förster Schreiber et al. (2018). The last panel of Figure 2.0.1 shows the integrated Hα map. The emission peaks off-center, on a region of $\sim$kiloparsec size in the southwest, and is faint in the central region of BX610 as expected from dust obscuration.

2.3 HST

We include HST imaging of the rest-frame optical light based on WFC3/IR observations using the F160W and F110W filters. A detailed description of the

[1] https://github.com/richteague/bettermoments

observations is described in Tacchella et al. (2015). We also use the stellar mass and visual extinction (A_V) maps derived based on optical to NIR broadband spectral energy distributions as described in the same study.

Chapter 3

Methods

3.1 Stacking the [CI] Spectra

Since one of our main goals is to analyze radial trends in the molecular gas content and excitation properties in BX610, we need to maximize the detectability of the CO $(4-3)$ and [CI] $(1-0)$ emission lines across the entire galaxy. However, the signal-to-noise ratio (S/N) of the [CI] $(1-0)$ emission line decreases more rapidly than that of the CO $(4-3)$ line towards the outer regions. To enhance the detection of the [CI] $(1-0)$ line, we employ a spectral stacking method as described by, for example, Schruba et al. (2011) and Villanueva et al. (2021).

The stacking procedure is as follows: First, we determine the central velocity of each spaxel in the CO $(4-3)$ cube. Next, each [CI] $(1-0)$ spaxel is shifted according to the CO $(4-3)$ velocity field, to align the spectrum of each line of sight to zero velocity. The spectra are then averaged into radial bins defined by the galactocentric radius, with a bin width of $0.09''$—half the beamsize of the data. This approach ensures that the radial bins do not oversample the radial profiles. To extract the line intensity, we fit a single-Gaussian profile to the averaged-stacked spectra. The uncertainties for each radial bin are calculated using the following equation,

$$u = \sigma\sqrt{N}\Delta v, \tag{3.1.1}$$

where σ is the RMS from the emission-free portion of the stacked spectrum, N is the number of channels included in the mask, and Δv is the channel width in km s^{-1}. To ensure reliable detection, we only consider [CI] $(1-0)$ averaged-stacked spectra that exceed the 5σ level. Using this method, we extend the detection of the [CI] $(1-0)$ line up to at least one stellar effective radius.

3.2 Molecular Gas Mass

Molecular gas masses are computed from the CO $(4-3)$ and [CI] $(1-0)$ line luminosities, which are defined by Solomon and Vanden Bout (2005) as,

$$L'_{\rm line}\left[{\rm K\ km\ s^{-1}\ pc^{2}}\right] = 3.25\times10^{7} S_{\rm line}\,\Delta v\ \nu_{\rm obs}^{-2}\ (1+z)^{-3}\ D_{\rm L}^{2}, \qquad (3.2.1)$$

where $S_{\rm line}\Delta v$ is the measured velocity-integrated line flux in Jy km s^{-1}, $\nu_{\rm obs}$ is the observed line frequency in GHz, z is the redshift of the source, and $D_{\rm L}$ is the luminosity distance in Mpc.

The total cold molecular gas mass, $M_{\rm mol}$, is then derived from the CO $(4-3)$ line luminosity as,

$$M_{\rm mol}\left[{\rm M_{\odot}}\right] = \alpha_{\rm CO}\ R_{14}\ L'_{\rm CO\ (4-3)}, \qquad (3.2.2)$$

where $\alpha_{\rm CO}$ is the luminosity-to-molecular-gas-mass conversion factor, including a 36% contribution from helium, and $R_{14} = L'_{\rm CO\ (1-0)}/L'_{\rm CO\ (4-3)}$ is the line luminosity ratio between the $J=4\rightarrow3$ and $J=1\rightarrow0$ transitions.

Several studies (e.g., Leroy et al., 2011; Genzel et al., 2012; Narayanan et al., 2012; Bolatto et al., 2013; Sandstrom et al., 2013) have shown that the $\alpha_{\rm CO}$ conversion factor can result in a wide range of values depending on the galaxy properties, including the density, temperature, and metallicity of the molecular clouds. While for local (U)LIRGs and starburst galaxies a value of $\alpha_{\rm CO} = 0.8\ {\rm M_{\odot}\ (K\ km\ s^{-1}\ pc^{2})^{-1}}$ is typically assumed (e.g., Downes and Solomon, 1998), high redshift star-forming galaxies at the massive end of the main-sequence tend to have $\alpha_{\rm CO}$ values comparable to the standard Milky Way value of $\alpha_{\rm MW} = 4.36\ {\rm M_{\odot}\ (K\ km\ s^{-1}\ pc^{2})^{-1}}$ (Bolatto et al., 2013; Tacconi et al., 2020).

To derive the $\alpha_{\rm CO}$ value for BX610, we follow the calibration presented in Genzel et al. (2015) (also adopted in Tacconi et al., 2018), which combines the recipes given by Genzel et al. (2012) and Bolatto et al. (2013) through the geometric mean of both empirical functions. The $\alpha_{\rm CO}$ value based on the metallicity of the gas is given by,

$$\alpha_{\rm CO} = \alpha_{\rm MW} \sqrt{10^{-1.27\times(12+\log{\rm (O/H)}-8.67)}} \sqrt{0.67 \exp{[0.36 \times 10^{-(12+\log{\rm (O/H)}-8.67)}]}} \tag{3.2.3}$$

where $12 + \log{\rm (O/H)}$ is the metallicity on the Pettini and Pagel (2004) calibration scale, denoted as,

$$12 + \log{\rm (O/H)}_{\rm PP04} = a - 0.087 \left[\log{(M_\star)} - b\right]^2, \tag{3.2.4}$$

with $a = 8.74 \pm 0.06$ and $b = (10.4 \pm 0.05) + (4.46 \pm 0.3) \times \log{(1+z)} - (1.78 \pm 0.4) \times [\log{(1+z)}]^2$ (Genzel et al., 2015, and references within). Based on the total stellar mass of BX610, we find a metallicity value of $12 + \log{\rm (O/H)} = 8.65 \pm 0.07$, which yields an $\alpha_{\rm CO} = 4.51 \pm 0.60$ $\rm M_\odot$ (K km s^{-1} pc^2)$^{-1}$.

The R_{14} line luminosity ratio converts the observed CO $(4-3)$ line luminosity into the CO $(1-0)$ line luminosity. Bolatto et al. (2015) recently conducted CO $(1-0)$ observations on BX610 using the JVLA and detect a total line luminosity of $L'_{\rm CO\ (1-0)} = (2.6 \pm 0.2) \times 10^{10}$ K km s^{-1} pc^2, which yields a line luminosity ratio of $R_{14} = 1.1 \pm 0.1$. Under these assumptions and values, we find a molecular gas mass of $M_{\rm mol} = (1.2 \pm 0.2) \times 10^{11}$ $\rm M_\odot$.

Alternatively, $M_{\rm mol}$ can be derived from the [CI] $(1-0)$ emission line (e.g., Weiß et al., 2005; Walter et al., 2011; Alaghband-Zadeh et al., 2013; Bothwell et al., 2017; Popping et al., 2017; Valentino et al., 2018), based on an estimated atomic mass of carbon, $M_{\rm [CI]}$, and the assumption of a given neutral atomic carbon abundance $X{\rm [CI]}/X{\rm [H_2]}$. The atomic carbon mass is estimated from the [CI] $(1-0)$ line luminosity emission following the formula presented by Weiß et al. (2005),

$$M_{\rm [CI]}\ \left[{\rm M_\odot}\right] = 5.706 \times 10^{-4}\ Q(T_{\rm ex})\ \frac{\exp{(T_1/T_{\rm ex})}}{3}\ L'_{\rm [CI]\ (1-0)}, \tag{3.2.5}$$

where $Q(T_{\rm ex}) = 1 + 3\exp{(-T_1/T_{\rm ex})} + 5\exp{(T_2/T_{\rm ex})}$ is the partition function, $T_{\rm ex}$ is the excitation temperature, and $T_1 = 23.6$ K and $T_2 = 62.5$ K are the transition energy levels above ground state. Brisbin et al. (2019) recently measured $T_{\rm ex}$ for BX610 based on the $L'_{\rm [CI]\ (2-1)} \big/ L'_{\rm [CI]\ (1-0)}$ line luminosity ratio and obtained a value of $T_{\rm ex} = 31.8 \pm 6.9$ K, which is comparable to the typical dust temperature of $T_{\rm dust} \sim 32$ K found in massive ($M_\star \sim 10^{11} - 10^{11.5}$ $\rm M_\odot$), main-sequence galaxies at $z \sim 2$ (Magnelli et al., 2014; Genzel et al., 2015; Schreiber et al., 2018). We then estimate an atomic carbon mass value of $M_{[\mathrm{CI}]} = (8.3 \pm 0.9) \times 10^6\ \mathrm{M}_\odot$. Valentino et al. (2018) study the value of the neutral atomic carbon abundance, $X[\mathrm{CI}]/X[\mathrm{H}_2] = M_{[\mathrm{CI}]}/6M_{\mathrm{H}_2}$, in a sample of main-sequence galaxies at $z \sim 1.2$ by comparing the molecular hydrogen masses derived from CO and dust, and report a span of values between $1 - 13 \times 10^{-5}$, with a weighted mean of 1.55×10^{-5}. Under these assumptions, we measure a molecular hydrogen mass of $M_{\mathrm{H}_2} = (9.5 \pm 0.7) \times 10^{10}\ \mathrm{M}_\odot$ and, as a result, a molecular gas mass of $M_{\mathrm{mol}} = (1.3 \pm 0.1) \times 10^{11}\ \mathrm{M}_\odot$, which is consistent with our CO-based measurement.

These CO- and [CI]-based molecular gas masses agree with the value reported previously by Bolatto et al. (2015), who estimated a molecular gas mass of $M_{\mathrm{mol}} = (1.1 \pm 0.1) \times 10^{11}\ \mathrm{M}_\odot$. However, it is a factor of ~ 2 lower than the value found by Brisbin et al. (2019), who reported a molecular gas mass of $M_{\mathrm{mol}} = (2.1 \pm 0.3) \times 10^{11}\ \mathrm{M}_\odot$. This could be explained because Brisbin et al. (2019), as described in Section 2.1, measured an ALMA Band 4 dust continuum that is a factor of ~ 2 larger than the value reported in this work and in Lee et al. (2024).

3.3 Star Formation Rate

We measure the SFR from the Hα line using the calibration by Kennicutt (1998) modified for a Chabrier (2003) initial mass function (IMF), as follows,

$$\mathrm{SFR}_{\mathrm{H}\alpha} \left[\mathrm{M}_\odot\ \mathrm{yr}^{-1}\right] = 4.7 \times 10^{-42}\ L_{\mathrm{H}\alpha,\,\mathrm{corr}}, \tag{3.3.1}$$

where $L_{\mathrm{H}\alpha,\,\mathrm{corr}}$ is the Hα luminosity in erg s^{-1} corrected for attenuation $A_{\mathrm{H}\alpha}$, i.e., $L_{\mathrm{H}\alpha,\,\mathrm{corr}} = L_{\mathrm{H}\alpha,\,\mathrm{obs}} \times 10^{0.4A_{\mathrm{H}\alpha}}$. For the attenuation $A_{\mathrm{H}\alpha}$, we use the extinction radial profiles measured by Tacchella et al. (2018) based on HST observations of the F438W (B) $-$ F814W (I) index color. We assume a $E(B-V)_{\mathrm{star}}/E(B-V)_{\mathrm{gas}}$ ratio of 0.44 (from Calzetti et al., 2010).

Additionally, in dusty environments such as the center of galaxies, the luminosity of young massive stars is frequently absorbed and then re-emitted in the IR, with an emission peak near 100 μm (e.g., Lutz et al., 2016). Therefore, the infrared emission can be a proxy for estimating the dust-obscured star formation. As can be seen from Figure 2.0.1, the molecular gas content as traced by the CO $(4-3)$ and [CI] $(1-0)$ transitions peaks at the center of the galaxy, however, the Hα line in this region is very faint. This is the result of strong dust obscuration in the center, where a correction based on the attenuation $A_{\mathrm{H}\alpha}$ measured from HST imaging is likely to significantly underestimate the total star formation activity. For this reason, in the central region of BX610, we use the ALMA dust continuum to measure the obscured star formation. First, we scale the ALMA Band 4 dust continuum flux to calculate the rest-frame 70 μm flux assuming a modified black-body (MBB, Casey, 2012) with a spectral emissivity index $\beta = 2$ and a dust temperature $T_{\rm dust} = 30$ K, as determined by Brisbin et al. (2019). The resulting flux is $S_{\rm cont,\,70\ \mu m} = 13.2$ mJy, consistent with the flux obtained from the MAGPHYS-derived Spectral Energy Distribution (SED) by Brisbin et al. (2019). Finally, we use the calibration by Calzetti et al. (2010) to measure the SFR based on the 70 μm continuum emission, which is given by,

$$\mathrm{SFR}_{70}\left[\mathrm{M}_{\odot}\ \mathrm{yr}^{-1}\right] = 5.9 \times 10^{-44}\ L_{70}, \tag{3.3.2}$$

where L_{70} is the luminosity at 70 μm.

Chapter 4

Results

4.1 Molecular Gas Excitation

With the development of wideband receivers that can simultaneously detect the CO $(4-3)$ and [CI] $(1-0)$ transitions in galaxies within certain redshift ranges (such as BX610 at $z \approx 2$), the $L'_{\mathrm{CO}\ (4-3)}\ /\ L'_{\mathrm{[CI]}\ (1-0)}$ line luminosity ratio has become an important tracer of molecular gas excitation (e.g., Alaghband-Zadeh et al., 2013; Bothwell et al., 2017; Valentino et al., 2018, 2020; Michiyama et al., 2021). This ratio is particularly useful because the excitation temperature of the [CI] $(1-0)$ line is only about 1.5 times higher than that of the CO $(2-1)$ line, and the critical density of the [CI] $(1-0)$ line is approximately 4.4 times lower than that of the CO $(1-0)$ transition (e.g., Carilli and Walter, 2013).

To date, most studies have focused on global measurements of the $L'_{\mathrm{CO}\ (4-3)}\ /\ L'_{\mathrm{[CI]}\ (1-0)}$ line luminosity ratio at high redshift. For example, in main-sequence star-forming galaxies at $z \sim 1$, Valentino et al. (2020) find an average value of $L'_{\mathrm{CO}\ (4-3)}\ /\ L'_{\mathrm{[CI]}\ (1-0)} = 2.13 \pm 0.31$. In the case of BX610, however, we now have the opportunity to explore excitation conditions on kiloparsec scales, extending out to one stellar effective radius, thanks to our stacking technique. The left panel of Figure 4.1.1 presents the $L'_{\mathrm{CO}\ (4-3)}\ /\ L'_{\mathrm{[CI]}\ (1-0)}$ line luminosity ratio map, normalized to the average value found in $z \sim 1$ main-sequence galaxies (Valentino et al., 2020). In the central region of BX610, the molecular gas is significantly more excited than in the outer regions, with a line ratio nearly twice the typical global value found in $z \sim 1$ main-sequence galaxies. Interestingly, the

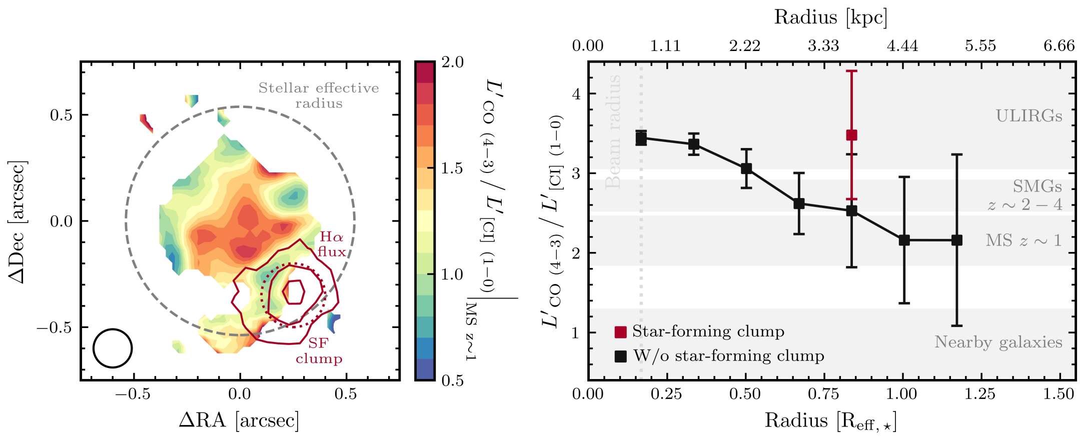

Figure 4.1.1: *Left:* $L'_{\mathrm{CO}\ (4-3)}$ / $L'_{\mathrm{[CI]}\ (1-0)}$ line luminosity ratio map normalized by the mean value found by Valentino et al. (2020) for main-sequence galaxies at $z \sim 1$. The galaxy's stellar effective radius is shown as the dotted gray circle. The red solid contours correspond to Hα fractional flux levels relative to the maximum of 0.5, 0.75, and 0.95, while the red dotted contour denotes the position of the star-forming clump. The filled circle at the bottom left corner indicates the beam size. *Right:* Radial profile of the line luminosity ratio as a function of the galaxy's stellar effective radius. The black squares with error bars show the mean value of the line luminosity ratio within each beam-sized bin, without considering the emission of the clump. The red square with the error bar shows the mean value of the line luminosity ratio within the clump. The gray-shaded areas are typical line luminosity ratio values, taken from the literature (e.g., Papadopoulos and Geach, 2012; Valentino et al., 2020). The vertical gray dotted line indicates the beam radius. We observe that the mean value in the central region is comparable to that of local ULIRGs, as well as the mean value in the star-forming clump, while the mean value in the outer disk is comparable to that of the main-sequence galaxies at $z \sim 1$.

spiral arm extending southward, next to the giant star-forming clump detected in Hα emission, exhibits a line ratio comparable to that of $z \sim 1$ main-sequence galaxies.

The right panel of Figure 4.1.1 displays the radial profile of the $L'_{\mathrm{CO}\ (4-3)}$ / $L'_{\mathrm{[CI]}\ (1-0)}$ line luminosity ratio, with the radius normalized to the effective stellar radius in the bottom x-axis. At each radius, the profile is calculated by taking the ratio of the summed CO $(4-3)$ line luminosities to the stacked [CI] $(1-0)$ line luminosities. The emission from the star-forming clump is masked (based on the area marked by the red dashed aperture on the left panel) and shown separately (in red). In the central region of BX610, the line luminosity ratio is comparable to that found in local (U)LIRGs (Papadopoulos and Geach, 2012). Moving outwards, at around $r \sim 0.5$ $R_{eff,\star}$, the ratio decreases to levels similar to those observed in SMGs at $z \sim 2-4$ (Valentino et al., 2020). Finally, in the range of $r \sim [0.75-1.25]$ $R_{eff,\star}$, the line luminosity ratio is comparable to the typical values found in main-sequence star-forming galaxies at $z \sim 1$ (Valentino et al., 2020). The star-forming clump, located at $r \sim 0.8$ $R_{eff,\star}$, exhibits a line luminosity ratio similar to that in the center of BX610, indicating elevated molecular gas excitation due to intense star formation. Notably, the global line luminosity ratio in BX610, $L'_{CO\ (4-3)} \,/\, L'_{[CI]\ (1-0)} = 2.7 \pm 0.7$, is consistent with that observed in $z \sim 1$ main-sequence galaxies (Valentino et al., 2020). This underscores the importance of spatially resolved observations in revealing the full range of molecular excitation conditions within galaxies, especially in regions of elevated star formation activity, such as central areas or extra-nuclear star-forming clumps.

4.2 Stellar, Molecular, and Star Formation Rate Radial Profiles

Figure 4.2.1 presents, from left to right, the radial profiles of stellar mass ($\Sigma_\star$), molecular gas mass (Σ_{mol}), and SFR (Σ_{SFR}) surface densities in BX610. Similar to Figure 4.1.1, we mask the emission from the star-forming clump in all three panels and represent it as a single red point. The middle panel shows the molecular gas radial profile based on CO emission. We choose the CO-based profile over the [CI]-based profile because CO emission extends farther across the disk, enabling the study of molecular gas surface density up to a radius of ~ 1.5 $R_{eff,\star}$. However, in the central region, the radial profile of the molecular gas, as traced by the CO $(4-3)$ and the [CI] $(1-0)$ emission line, is comparable. In the right panel, we present the radial profile of the SFR derived from extinction-corrected Hα emission (black squares). In the central region ($\lesssim 0.5$ $R_{eff,\star}$), where ALMA detects dust continuum and Hα emission is faint, the dust continuum-based SFR (green squares) is approximately five times higher than the extinction-corrected Hα-based SFR. This discrepancy is likely due to the optical extinction correction from Tacchella et al. (2018) being insufficient to fully account for the significant dust obscuration in the central region of BX610. However, it is important to note that the infrared-based SFR here is derived from dust continuum observations

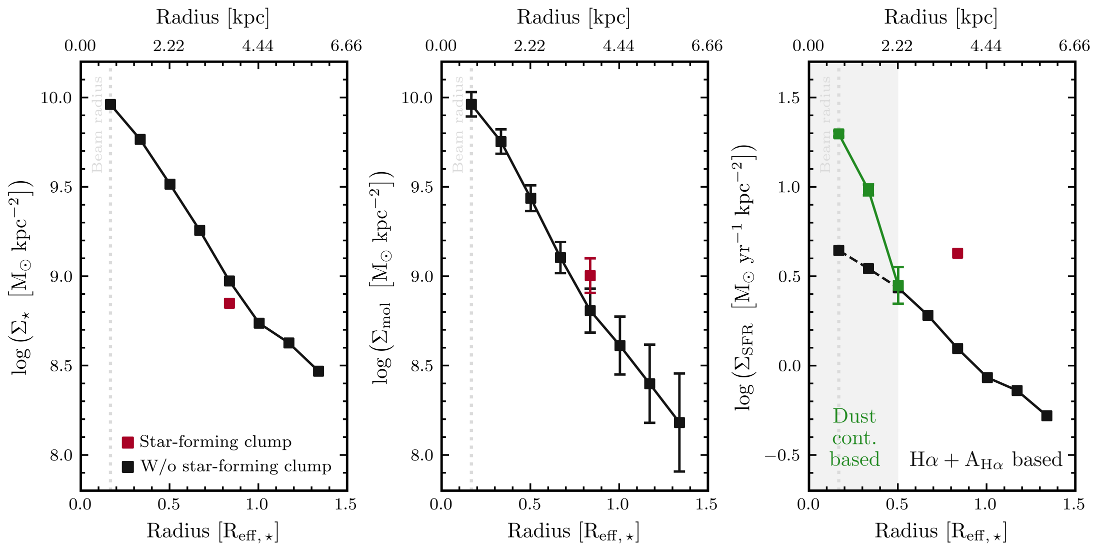

Figure 4.2.1: Radial profiles of the stellar mass (left), molecular gas mass (middle), and SFR (right) surface densities of BX610, plotted with the same logarithmic dynamic range to facilitate comparison. Colors indicate the same as in Figure 4.1.1. In the right panel, green squares above the gray-shaded area are derived from the rest-frame 630 μm dust continuum emission, while black squares are derived from Hα corrected by dust attenuation profile of Tacchella et al. (2018). The vertical gray dotted line indicates the beam radius. We observe in the central region of the right panel that the $\mathrm{SFR_{H\alpha}}$ surface density is clearly underestimated in comparison with the $\mathrm{SFR_{dust}}$ surface density.

at a wavelength away from the peak of the infrared SED, introducing significant uncertainties. To obtain a more accurate measurement of the total SFR in the central region of BX610, ALMA dust continuum observations closer to the SED peak, such as those in Bands 8 or 9 (rest-frame $\sim 150\ \mu$m), are required.

Additionally, we observe that both the star-forming clump and the disk have similar stellar mass values at $r \sim 0.8\ \mathrm{R_{eff,\star}}$. However, the clump shows higher average values of Σ_{mol} and Σ_{SFR} at this galactocentric distance. This suggests that the elevated star formation activity in the clump is a result of the greater concentration of molecular gas compared to other regions of the disk. The similarity in $\Sigma_\star$ values between the disk and the clump at $r \sim 0.8\ \mathrm{R_{eff,\star}}$ suggests that the star formation activity is so recent that it has not yet led to a significant increase in the stellar mass of the clump region.

The left panel of Figure 4.2.2 shows the radial profile of the molecular gas fraction, $\mu_{\mathrm{mol}} = M_{\mathrm{mol}}/M_\star$, which serves as an indicator of the gas available for star formation relative to the existing stellar content. We observe that in the central region

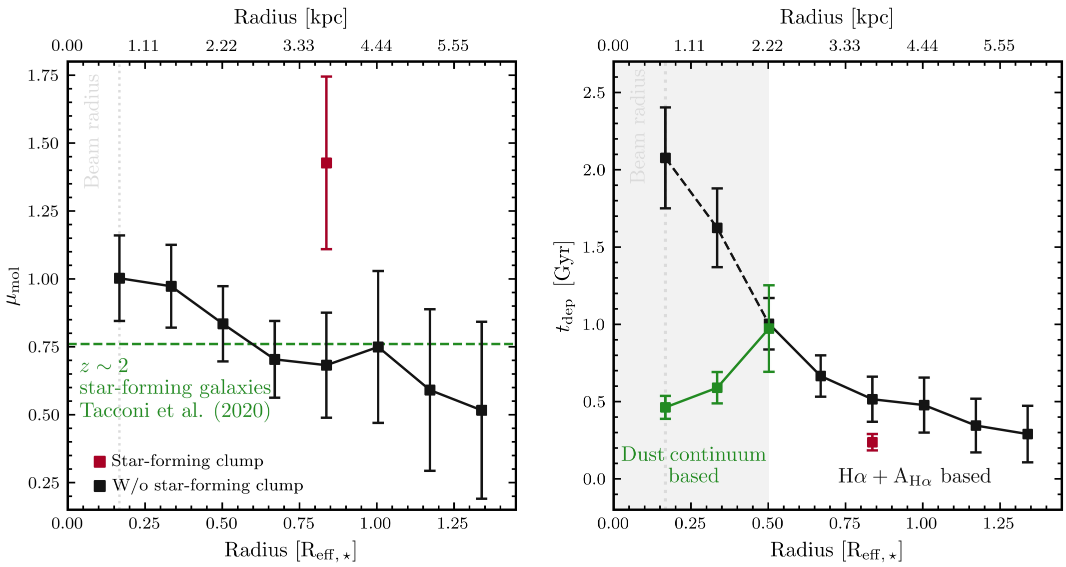

Figure 4.2.2: Radial profiles of the molecular gas fraction (left) and the molecular gas depletion time (right) in BX610. Colors indicate the same as in Figure 4.2.1. The vertical gray dotted line indicates the beam radius. In the left panel, the green dashed line indicates the average molecular gas fraction measured by Tacconi et al. (2020) for main-sequence galaxies at $z \sim 2$.

($\lesssim 0.4$ $R_{eff,\star}$) of BX610, the molecular gas fraction is close to unity, and then it decreases to $\mu_{mol} \approx 0.5$ beyond one stellar effective radius. The global molecular gas fraction in BX610 is comparable to that measured in main-sequence star-forming galaxies at $z \sim 2$ ($\mu_{mol} \approx 0.75$; Tacconi et al., 2020), but this is a result of averaging the high molecular gas fraction of $\mu_{mol} \approx 1$ measured at the central ~ 2 kpc of BX610 with the $\mu_{mol} \approx 0.5$ in the outer parts. The star-forming clump in the southwest has an even higher molecular gas fraction than the central region ($\mu_{mol} \approx 1.4$), which is consistent with the elevated star formation activity traced by the Hα line.

The right panel of Figure 4.2.2 shows the molecular gas depletion time, $t_{dep} = \Sigma_{mol}/\Sigma_{SFR}$, which represents the time required to deplete the molecular gas reservoirs at the current rate of star formation. In the inner ~ 0.5 $R_{eff,\star}$ (~ 2 kpc) radius, the depletion timescale varies depending on whether we assume the extinction-corrected Hα-based (black curve) or the dust continuum-based SFR (green curve). Given the elevated concentration of molecular gas in the center and the strong dust continuum detected with ALMA, we believe the latter is more representative of the total SFR in the nuclear region of BX610. If that is the case, then the depletion time decreases towards the center, reaching values of

≈ 450 Myr, which is consistent with depletion timescales measured in massive, star-forming galaxies at $z \sim 2$ (e.g., Tacconi et al., 2020). The star-forming clump is the region with the lowest depletion time in BX610: the current level of star formation activity should exhaust the molecular gas in only ≈ 250 Myr.

Placing these results in the broader context of galaxy evolution at cosmic noon, we infer that BX610 is likely in a phase where the rapid inflow of molecular gas into the central region, as reported by Genzel et al. (2023), has created a gas-rich nucleus ($\mu_{\rm mol} \approx 1$), driving a high central star formation rate. This phase is commonly referred to as the wet compaction (Dekel and Burkert, 2014; Zolotov et al., 2015; Tacchella et al., 2016). Following this phase, galaxies are expected to cease star formation in their centers before the outskirts, driven by a steep decline in the molecular gas fraction in the central kiloparsec region—a pattern opposite to what is observed in BX610 but consistent with findings in compact star-forming galaxies at $z \sim 2$ in the process of inside-out quenching (e.g., Spilker et al., 2019).

4.3 Kennicutt-Schmidt Law

We now explore the relationship between molecular gas surface density ($\Sigma_{\rm mol}$) and star formation rate surface density ($\Sigma_{\rm SFR}$), as described by the Kennicutt-Schmidt law (Schmidt, 1959; Kennicutt, 1998). This relationship is key to understanding how efficiently cold gas is converted into stars across different environments (e.g., Genzel et al., 2010; Freundlich et al., 2013; Tacconi et al., 2013; Hodge et al., 2015; Chen et al., 2017; Sun et al., 2023; Villanueva et al., 2024). Figure 4.3.1 shows the resolved KS relation for BX610, with data points color-coded by radial distance and distinguished by shape according to specific regions within the galaxy. The figure is based on measurements from apertures across BX610, each with a diameter of $0.18''$ (matching the beam size) and centers separated by $0.09''$ to minimize flux loss from overlapping apertures. For the disk and clump regions, SFR values are derived from extinction-corrected Hα fluxes, while for the central regions, they are based on the ALMA dust continuum emission.

Overall, the ~kiloparsec-scale regions in BX610 align with the trend observed in spatially resolved studies of other massive, star-forming galaxies at $z \sim 1-2$ (Tacconi et al., 2013; Freundlich et al., 2013; Genzel et al., 2013). Disk regions

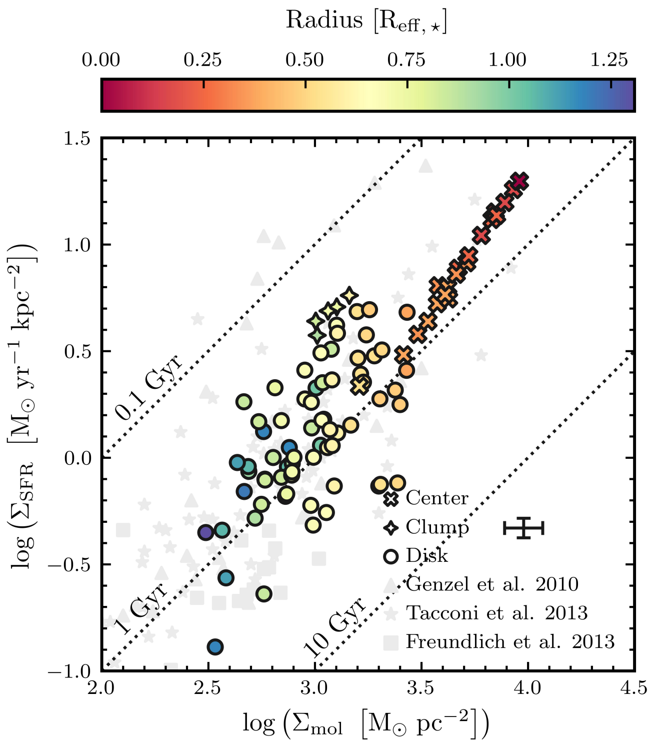

Figure 4.3.1: Kennicutt-Schmidt diagram of BX610 for 0.18″ overlapped apertures of the center (crosses), the clump (stars), and the disk (circles). The color bar indicates the distance to the center as a function of the stellar effective radius. A typical error bar is shown in the bottom right corner. The dotted diagonal lines correspond to constant gas depletion times of 0.1, 1, and 10 Gyr from top to bottom. The gray data points from Genzel et al. (2010) and Tacconi et al. (2013) are indicated for comparison with whole galaxies, while the data points from Freundlich et al. (2013) are for spatially resolved main-sequence galaxies at $z \sim 1$.

(circles) exhibit depletion timescales that scatter around ~ 1 Gyr, with variations of about a factor of $\sim$ 2. As regions approach the center of BX610 (crosses), depletion times shorten, reaching close to ~ 450 Myr. Notably, the extra-nuclear star-forming clump (stars) is the region in BX610 with the highest star formation efficiency, with a short depletion time of only ~ 250 Myr. Applying an ordinary least-squares bisector fit to all the regions in BX610, we find that $\log(\Sigma_{SFR}) = (1.27 \pm 0.05) \times \log(\Sigma_{mol}) - (3.68 \pm 0.17)$.

Similar to the case of the star-forming galaxy EGS13011166 at $z \approx 1.5$ (Genzel et al., 2013), the fit will depend on the way the correction for dust obscuration is implemented. For EGS13011166, the slope varies from 0.8 to 1.7 depending on the adopted extinction model, but for the preferred mixed-dust gas model, Genzel et al. (2013) find a super-linear slope of $N = 1.14 \pm 0.1$, comparable within the uncertainties and assumptions with the measured slope in BX610 of $N = 1.27 \pm 0.05$.

Chapter 5

Conclusions

We have conducted deep, high-angular-resolution (0.18″) ALMA Band 4 observations targeting the molecular gas traced by the CO $(4-3)$ and [CI] $(1-0)$ transitions in BX610, a massive main-sequence galaxy at $z = 2.21$. These observations, combined with VLT/SINFONI AO-assisted Hα emission line data (Förster Schreiber et al., 2018), have allowed us to characterize the molecular gas properties and star formation activity on ∼kiloparsec scales, spanning from the central regions to at least $\sim$ 1.5 ($\sim$7 kpc) stellar effective radius in this typical star-forming galaxy at cosmic noon.

Our key findings are as follows:

1. By using the $L'_{\rm CO\ (4-3)}/L'_{\rm [CI]\ (1-0)}$ line luminosity ratio as a tracer of molecular gas excitation in BX610, we find that the central region and the extra-nuclear, giant star-forming clump exhibit excitation levels comparable to those observed in nearby (U)LIRGs (Papadopoulos and Geach, 2012). Beyond $\sim$0.5 $R_{\rm eff,\star}$, and on average across the disk, the molecular gas excitation conditions in BX610 resemble those typically found in normal star-forming galaxies at $z \sim 1$ (e.g., Valentino et al., 2020).
2. The molecular gas fraction measured in the inner $\sim$2 kpc ($\sim$0.5 $R_{\rm eff,\star}$) of BX610 and the giant star-forming clump in the southwest is high ($\mu_{\rm mol} \approx 1$), resulting in intense star formation activity. Overall, the molecular gas fraction in the disk ($\mu_{\rm mol} \approx 0.5-0.7$) is comparable to that globally measured in main-sequence, massive star-forming galaxies at $z \approx 2$ (e.g., Tacconi et al., 2020). The molecular gas depletion times measured in the central region and

in the giant star-forming clump are ~ 450 Myr and ~ 250 Myr, respectively.

3. The rapid transport of molecular gas to the central region of BX610 (Genzel et al., 2023), combined with the high central molecular gas fraction and short depletion timescale, suggests that BX610 may be undergoing a phase similar to the wet compaction scenario described in models by Dekel and Burkert (2014), Zolotov et al. (2015), and Tacchella et al. (2018). In this phase, the concentration of gas in the galaxy's core drives intense star formation, which eventually leads to the inside-out quenching of star formation.

4. The ~kiloparsec-scale regions in BX610 exhibit significant variations but generally align with the spatially-resolved KS relation observed in other massive, star-forming galaxies at $z \sim 1-2$ (e.g., Freundlich et al., 2013; Genzel et al., 2013; Tacconi et al., 2013). The overall slope and the depletion timescale measured in BX610 are $N = 1.27 \pm 0.05$ and $t_{\rm dep} \approx 800 \pm 400$ Myr, respectively.

In summary, the deep, spatially-resolved ALMA and VLT/SINFONI observations of BX610 provide one of the most detailed maps of molecular gas and star formation activity in a main-sequence, star-forming galaxy at cosmic noon. However, the absence of reliable measurements of obscured star formation in the central region limits our ability to fully interpret its physical conditions. Future ALMA observations at wavelengths closer to the SED peak (Band 8 or Band 9) or measurements of the Paschen-α line with JWST/MIRI are essential for addressing this issue and obtaining a more comprehensive understanding of the BX610 central region.

References

Alaghband-Zadeh, S., Chapman, S. C., Swinbank, A. M., Smail, I., Danielson, A. L. R., Decarli, R., Ivison, R. J., Meijerink, R., Weiss, A., and van der Werf, P. P. (2013). Using [C I] to probe the interstellar medium in z $\sim$ 2.5 sub-millimeter galaxies. *MNRAS*, 435(2):1493–1510.

Aravena, M., Hodge, J. A., Wagg, J., Carilli, C. L., Daddi, E., Dannerbauer, H., Lentati, L., Riechers, D. A., Sargent, M., and Walter, F. (2014). CO(1-0) line imaging of massive star-forming disc galaxies at z=1.5-2.2. *MNRAS*, 442(1):558–564.

Bisbas, T. G., Papadopoulos, P. P., and Viti, S. (2015). Effective Destruction of CO by Cosmic Rays: Implications for Tracing H_2 Gas in the Universe. *ApJ*, 803(1):37.

Bisbas, T. G., van Dishoeck, E. F., Papadopoulos, P. P., Szűcs, L., Bialy, S., and Zhang, Z.-Y. (2017). Cosmic-ray Induced Destruction of CO in Star-forming Galaxies. *ApJ*, 839(2):90.

Bolatto, A. D., Warren, S. R., Leroy, A. K., Tacconi, L. J., Bouché, N., Förster Schreiber, N. M., Genzel, R., Cooper, M. C., Fisher, D. B., Combes, F., García-Burillo, S., Burkert, A., Bournaud, F., Weiss, A., Saintonge, A., Wuyts, S., and Sternberg, A. (2015). High-resolution Imaging of PHIBSS z $\sim$ 2 Main-sequence Galaxies in CO J = 1 $\rightarrow$ 0. *ApJ*, 809(2):175.

Bolatto, A. D., Wolfire, M., and Leroy, A. K. (2013). The CO-to-H_2 Conversion Factor. *ARA&A*, 51(1):207–268.

Bolatto, A. D., Wong, T., Utomo, D., Blitz, L., Vogel, S. N., Sánchez, S. F., Barrera-Ballesteros, J., Cao, Y., Colombo, D., Dannerbauer, H., García-Benito, R., Herrera-Camus, R., Husemann, B., Kalinova, V., Leroy, A. K., Leung, G., Levy, R. C., Mast, D., Ostriker, E., Rosolowsky, E., Sandstrom, K. M., Teuben, P., van de Ven, G., and Walter, F. (2017). The EDGE-CALIFA Survey: Interferometric Observations of 126 Galaxies with CARMA. *ApJ*, 846(2):159.

Boogaard, L. A., Bouwens, R. J., Riechers, D., van der Werf, P., Bacon, R., Matthee, J., Stefanon, M., Feltre, A., Maseda, M., Inami, H., Aravena, M., Brinchmann, J., Carilli, C., Contini, T., Decarli, R., González-López, J., Nanayakkara, T., and Walter, F. (2021). Measuring the Average Molecular Gas Content of Star-forming Galaxies at z = 3-4. *ApJ*, 916(1):12.

Bothwell, M. S., Aguirre, J. E., Aravena, M., Bethermin, M., Bisbas, T. G., Chapman, S. C., De Breuck, C., Gonzalez, A. H., Greve, T. R., Hezaveh, Y., Ma, J., Malkan, M., Marrone, D. P., Murphy, E. J., Spilker, J. S., Strandet, M., Vieira, J. D., and Weiß, A. (2017). ALMA observations of atomic carbon in z ~ 4 dusty star-forming galaxies. *MNRAS*, 466(3):2825–2841.

Brinchmann, J., Charlot, S., White, S. D. M., Tremonti, C., Kauffmann, G., Heckman, T., and Brinkmann, J. (2004). The physical properties of star-forming galaxies in the low-redshift Universe. *MNRAS*, 351(4):1151–1179.

Brisbin, D., Aravena, M., Daddi, E., Dannerbauer, H., Decarli, R., González-López, J., Riechers, D., and Wagg, J. (2019). Neutral carbon and highly excited CO in a massive star-forming main sequence galaxy at z = 2.2. *A&A*, 628:A104.

Calzetti, D., Wu, S. Y., Hong, S., Kennicutt, R. C., Lee, J. C., Dale, D. A., Engelbracht, C. W., van Zee, L., Draine, B. T., Hao, C. N., Gordon, K. D., Moustakas, J., Murphy, E. J., Regan, M., Begum, A., Block, M., Dalcanton, J., Funes, J., Gil de Paz, A., Johnson, B., Sakai, S., Skillman, E., Walter, F., Weisz, D., Williams, B., and Wu, Y. (2010). The Calibration of Monochromatic Far-Infrared Star Formation Rate Indicators. *ApJ*, 714(2):1256–1279.

Carilli, C. L. and Walter, F. (2013). Cool Gas in High-Redshift Galaxies. *ARA&A*, 51(1):105–161.

Casey, C. M. (2012). Far-infrared spectral energy distribution fitting for galaxies near and far. *MNRAS*, 425(4):3094–3103.

Chabrier, G. (2003). Galactic Stellar and Substellar Initial Mass Function. *PASP*, 115(809):763–795.

Chen, C.-C., Hodge, J. A., Smail, I., Swinbank, A. M., Walter, F., Simpson, J. M., Calistro Rivera, G., Bertoldi, F., Brandt, W. N., Chapman, S. C., da Cunha, E., Dannerbauer, H., De Breuck, C., Harrison, C. M., Ivison, R. J., Karim, A., Knudsen, K. K., Wardlow, J. L., Weiß, A., and van der Werf, P. P. (2017). A Spatially Resolved Study of Cold Dust, Molecular Gas, H II Regions, and Stars in the z = 2.12 Submillimeter Galaxy ALESS67.1. *ApJ*, 846(2):108.

Daddi, E., Alexander, D. M., Dickinson, M., Gilli, R., Renzini, A., Elbaz, D., Cimatti, A., Chary, R., Frayer, D., Bauer, F. E., Brandt, W. N., Giavalisco, M., Grogin, N. A., Huynh, M., Kurk, J., Mignoli, M., Morrison, G., Pope, A., and Ravindranath, S. (2007). Multiwavelength Study of Massive Galaxies at z~2. II. Widespread Compton-thick Active Galactic Nuclei and the Concurrent Growth of Black Holes and Bulges. *ApJ*, 670(1):173–189.

Daddi, E., Bournaud, F., Walter, F., Dannerbauer, H., Carilli, C. L., Dickinson, M., Elbaz, D., Morrison, G. E., Riechers, D., Onodera, M., Salmi, F., Krips, M., and Stern, D. (2010). Very High Gas Fractions and Extended Gas Reservoirs in z = 1.5 Disk Galaxies. *ApJ*, 713(1):686–707.

Dekel, A. and Burkert, A. (2014). Wet disc contraction to galactic blue nuggets and quenching to red nuggets. *MNRAS*, 438(2):1870–1879.

Downes, D. and Solomon, P. M. (1998). Rotating Nuclear Rings and Extreme Starbursts in Ultraluminous Galaxies. *ApJ*, 507(2):615–654.

Elbaz, D., Daddi, E., Le Borgne, D., Dickinson, M., Alexander, D. M., Chary, R. R., Starck, J. L., Brandt, W. N., Kitzbichler, M., MacDonald, E., Nonino, M., Popesso, P., Stern, D., and Vanzella, E. (2007). The reversal of the star formation-density relation in the distant universe. *A&A*, 468(1):33–48.

Elbaz, D., Dickinson, M., Hwang, H. S., Díaz-Santos, T., Magdis, G., Magnelli, B., Le Borgne, D., Galliano, F., Pannella, M., Chanial, P., Armus, L., Charmandaris, V., Daddi, E., Aussel, H., Popesso, P., Kartaltepe, J., Altieri, B., Valtchanov, I., Coia, D., Dannerbauer, H., Dasyra, K., Leiton, R., Mazzarella, J., Alexander, D. M., Buat, V., Burgarella, D., Chary, R. R., Gilli, R., Ivison, R. J., Juneau, S., Le Floc'h, E., Lutz, D., Morrison, G. E., Mullaney, J. R., Murphy, E., Pope, A., Scott, D., Brodwin, M., Calzetti, D., Cesarsky, C., Charlot, S., Dole, H., Eisenhardt, P., Ferguson, H. C., Förster Schreiber, N., Frayer, D., Giavalisco, M., Huynh, M., Koekemoer, A. M., Papovich, C., Reddy, N., Surace, C., Teplitz, H., Yun, M. S., and Wilson, G. (2011). GOODS-Herschel: an infrared main sequence for star-forming galaxies. *A&A*, 533:A119.

Erb, D. K., Steidel, C. C., Shapley, A. E., Pettini, M., Reddy, N. A., and Adelberger, K. L. (2006). The Stellar, Gas, and Dynamical Masses of Star-forming Galaxies at z ~2. *ApJ*, 646(1):107–132.

Förster Schreiber, N. M., Genzel, R., Bouché, N., Cresci, G., Davies, R., Buschkamp, P., Shapiro, K., Tacconi, L. J., Hicks, E. K. S., Genel, S., Shapley, A. E., Erb, D. K., Steidel, C. C., Lutz, D., Eisenhauer, F., Gillessen, S., Sternberg, A., Renzini, A., Cimatti, A., Daddi, E., Kurk, J., Lilly, S., Kong, X., Lehnert, M. D., Nesvadba, N., Verma, A., McCracken, H., Arimoto, N., Mignoli, M., and Onodera, M. (2009). The SINS Survey: SINFONI Integral Field Spectroscopy of z ~2 Star-forming Galaxies. *ApJ*, 706(2):1364–1428.

Förster Schreiber, N. M., Genzel, R., Newman, S. F., Kurk, J. D., Lutz, D., Tacconi, L. J., Wuyts, S., Bandara, K., Burkert, A., Buschkamp, P., Carollo, C. M., Cresci, G., Daddi, E., Davies, R., Eisenhauer, F., Hicks, E. K. S., Lang, P., Lilly, S. J., Mainieri, V., Mancini, C., Naab, T., Peng, Y., Renzini, A., Rosario, D., Shapiro Griffin, K., Shapley, A. E., Sternberg, A., Tacchella, S., Vergani, D., Wisnioski, E., Wuyts, E., and Zamorani, G. (2014). The Sins/zC-Sinf Survey of z ~2 Galaxy Kinematics: Evidence for Powerful Active Galactic Nucleus-Driven Nuclear Outflows in Massive Star-Forming Galaxies. *ApJ*, 787(1):38.

Förster Schreiber, N. M., Renzini, A., Mancini, C., Genzel, R., Bouché, N., Cresci, G., Hicks, E. K. S., Lilly, S. J., Peng, Y., Burkert, A., Carollo, C. M., Cimatti, A., Daddi, E., Davies, R. I., Genel, S., Kurk, J. D., Lang, P., Lutz, D., Mainieri, V., McCracken, H. J., Mignoli, M., Naab, T., Oesch, P., Pozzetti, L., Scodeggio, M., Shapiro Griffin, K., Shapley, A. E., Sternberg, A., Tacchella, S., Tacconi, L. J., Wuyts, S., and Zamorani, G. (2018). The SINS/zC-SINF Survey of z $\sim$ 2 Galaxy Kinematics: SINFONI Adaptive Optics-assisted Data and Kiloparsec-scale Emission-line Properties. *ApJS*, 238(2):21.

Förster Schreiber, N. M., Shapley, A. E., Erb, D. K., Genzel, R., Steidel, C. C., Bouché, N., Cresci, G., and Davies, R. (2011a). Constraints on the Assembly and Dynamics of Galaxies. I. Detailed Rest-frame Optical Morphologies on Kiloparsec Scale of z ~2 Star-forming Galaxies. *ApJ*, 731(1):65.

Förster Schreiber, N. M., Shapley, A. E., Genzel, R., Bouché, N., Cresci, G., Davies, R., Erb, D. K., Genel, S., Lutz, D., Newman, S., Shapiro, K. L., Steidel, C. C., Sternberg, A., and Tacconi, L. J. (2011b). Constraints on the Assembly and Dynamics of Galaxies. II. Properties of Kiloparsec-scale Clumps in Rest-frame Optical Emission of z ~2 Star-forming Galaxies. *ApJ*, 739(1):45.

Freundlich, J., Combes, F., Tacconi, L. J., Cooper, M. C., Genzel, R., Neri, R., Bolatto, A., Bournaud, F., Burkert, A., Cox, P., Davis, M., Förster Schreiber, N. M., Garcia-Burillo, S., Gracia-Carpio, J., Lutz, D., Naab, T., Newman, S., Sternberg, A., and Weiner, B. (2013). Towards a resolved Kennicutt-Schmidt law at high redshift. *A&A*, 553:A130.

Genzel, R., Jolly, J. B., Liu, D., Price, S. H., Lee, L. L., Förster Schreiber, N. M., Tacconi, L. J., Herrera-Camus, R., Barfety, C., Burkert, A., Cao, Y., Davies, R. I., Dekel, A., Lee, M. M., Lutz, D., Naab, T., Neri, R., Nestor Shachar, A., Pastras, S., Pulsoni, C., Renzini, A., Schuster, K., Shimizu, T. T., Stanley, F., Sternberg, A., and Übler, H. (2023). Evidence for Large-scale, Rapid Gas Inflows in z 2 Star-forming Disks. *ApJ*, 957(1):48.

Genzel, R., Tacconi, L. J., Combes, F., Bolatto, A., Neri, R., Sternberg, A., Cooper, M. C., Bouché, N., Bournaud, F., Burkert, A., Comerford, J., Cox, P., Davis, M., Förster Schreiber, N. M., Garcia-Burillo, S., Gracia-Carpio, J., Lutz, D., Naab, T., Newman, S., Saintonge, A., Shapiro, K., Shapley, A., and Weiner, B. (2012). The Metallicity Dependence of the CO $\rightarrow$ H_2 Conversion Factor in z $>=$ 1 Star-forming Galaxies. *ApJ*, 746(1):69.

Genzel, R., Tacconi, L. J., Gracia-Carpio, J., Sternberg, A., Cooper, M. C., Shapiro, K., Bolatto, A., Bouché, N., Bournaud, F., Burkert, A., Combes, F., Comerford, J., Cox, P., Davis, M., Förster Schreiber, N. M., Garcia-Burillo, S., Lutz, D., Naab, T., Neri, R., Omont, A., Shapley, A., and Weiner, B. (2010). A study of the gas-star formation relation over cosmic time. *MNRAS*, 407(4):2091–2108.

Genzel, R., Tacconi, L. J., Kurk, J., Wuyts, S., Combes, F., Freundlich, J., Bolatto, A., Cooper, M. C., Neri, R., Nordon, R., Bournaud, F., Burkert, A., Comerford, J., Cox, P., Davis, M., Förster Schreiber, N. M., García-Burillo, S., Gracia-Carpio, J., Lutz, D., Naab, T., Newman, S., Saintonge, A., Shapiro Griffin, K., Shapley, A., Sternberg, A., and Weiner, B. (2013). Phibss: Molecular Gas, Extinction, Star Formation, and Kinematics in the z = 1.5 Star-forming Galaxy EGS13011166. *ApJ*, 773(1):68.

Genzel, R., Tacconi, L. J., Lutz, D., Saintonge, A., Berta, S., Magnelli, B., Combes, F., García-Burillo, S., Neri, R., Bolatto, A., Contini, T., Lilly, S., Boissier, J., Boone, F., Bouché, N., Bournaud, F., Burkert, A., Carollo, M., Colina, L., Cooper, M. C., Cox, P., Feruglio, C., Förster Schreiber, N. M., Freundlich, J., Gracia-Carpio, J., Juneau, S., Kovac, K., Lippa, M., Naab, T., Salome, P., Renzini, A., Sternberg, A., Walter, F., Weiner, B., Weiss, A., and Wuyts, S. (2015). Combined CO and Dust Scaling Relations of Depletion Time and Molecular Gas Fractions with Cosmic Time, Specific Star-formation Rate, and Stellar Mass. *ApJ*, 800(1):20.

Glover, S. C. O. and Clark, P. C. (2016). Is atomic carbon a good tracer of molecular gas in metal-poor galaxies? *MNRAS*, 456(4):3596–3609.

Glover, S. C. O., Clark, P. C., Micic, M., and Molina, F. (2015). Modelling [C I] emission from turbulent molecular clouds. *MNRAS*, 448(2):1607–1627.

Henríquez-Brocal, K., Herrera-Camus, R., Tacconi, L., Genzel, R., Bolatto, A., Bovino, S., Demarco, R., Förster Schreiber, N., Lee, M., Lutz, D., and Rubio, M. (2022). Molecular gas properties of Q1700-MD94: A massive main-sequence galaxy at z $\approx$ 2. *A&A*, 657:L15.

Hodge, J. A., Riechers, D., Decarli, R., Walter, F., Carilli, C. L., Daddi, E., and Dannerbauer, H. (2015). The Kiloparsec-scale Star Formation Law at Redshift 4: Widespread, Highly Efficient Star Formation in the Dust-obscured Starburst Galaxy GN20. *ApJ*, 798(1):L18.

Hopkins, A. M. and Beacom, J. F. (2006). On the Normalization of the Cosmic Star Formation History. *ApJ*, 651(1):142–154.

Ikeda, M., Oka, T., Tatematsu, K., Sekimoto, Y., and Yamamoto, S. (2002). The Distribution of Atomic Carbon in the Orion Giant Molecular Cloud 1. *ApJS*, 139(2):467–485.

Ikeda, R., Tadaki, K.-i., Iono, D., Kodama, T., Chan, J. C. C., Hatsukade, B., Hayashi, M., Izumi, T., Kohno, K., Koyama, Y., Shimakawa, R., Suzuki, T. L., Tamura, Y., and Tanaka, I. (2022). High-resolution ALMA Study of CO J = 2-1 Line and Dust Continuum Emissions in Cluster Galaxies at z = 1.46. *ApJ*, 933(1):11.

Kennicutt, Robert C., J. (1998). Star Formation in Galaxies Along the Hubble Sequence. *ARA&A*, 36:189–232.

Kulesa, C. A., Hungerford, A. L., Walker, C. K., Zhang, X., and Lane, A. P. (2005). Large-Scale CO and [C I] Emission in the ρ Ophiuchi Molecular Cloud. *ApJ*, 625(1):194–209.

Lee, M. M., Steidel, C. C., Brammer, G., Förster-Schreiber, N., Renzini, A., Liu, D., Herrera-Camus, R., Naab, T., Price, S. H., Übler, H., Arriagada-Neira, S., and Magdis, G. (2024). High dust content of a quiescent galaxy at z 2 revealed by deep ALMA observation. *MNRAS*, 527(4):9529–9547.

Lee, M. M., Tanaka, I., Iono, D., Kawabe, R., Kodama, T., Kohno, K., Saito, T., and Tamura, Y. (2021). Revisited Cold Gas Content with Atomic Carbon [C I] in z = 2.5 Protocluster Galaxies. *ApJ*, 909(2):181.

Leroy, A. K., Bolatto, A., Gordon, K., Sandstrom, K., Gratier, P., Rosolowsky, E., Engelbracht, C. W., Mizuno, N., Corbelli, E., Fukui, Y., and Kawamura, A. (2011). The CO-to-H_2 Conversion Factor from Infrared Dust Emission across the Local Group. *ApJ*, 737(1):12.

Lilly, S. J., Le Fevre, O., Hammer, F., and Crampton, D. (1996). The Canada-France Redshift Survey: The Luminosity Density and Star Formation History of the Universe to Z approximately 1. *ApJ*, 460:L1.

Lutz, D., Berta, S., Contursi, A., Förster Schreiber, N. M., Genzel, R., Graciá-Carpio, J., Herrera-Camus, R., Netzer, H., Sturm, E., Tacconi, L. J., Tadaki, K., and Veilleux, S. (2016). The far-infrared emitting region in local galaxies and QSOs: Size and scaling relations. *A&A*, 591:A136.

Madau, P. and Dickinson, M. (2014). Cosmic Star-Formation History. *ARA&A*, 52:415–486.

Madau, P., Ferguson, H. C., Dickinson, M. E., Giavalisco, M., Steidel, C. C., and Fruchter, A. (1996). High-redshift galaxies in the Hubble Deep Field: colour selection and star formation history to z~4. *MNRAS*, 283(4):1388–1404.

Magnelli, B., Lutz, D., Saintonge, A., Berta, S., Santini, P., Symeonidis, M., Altieri, B., Andreani, P., Aussel, H., Béthermin, M., Bock, J., Bongiovanni, A., Cepa, J., Cimatti, A., Conley, A., Daddi, E., Elbaz, D., Förster Schreiber, N. M., Genzel, R., Ivison, R. J., Le Floc'h, E., Magdis, G., Maiolino, R., Nordon, R., Oliver, S. J., Page, M., Pérez García, A., Poglitsch, A., Popesso, P., Pozzi, F., Riguccini, L., Rodighiero, G., Rosario, D., Roseboom, I., Sanchez-Portal, M., Scott, D., Sturm, E., Tacconi, L. J., Valtchanov, I., Wang, L., and Wuyts, S. (2014). The evolution of the dust temperatures of galaxies in the SFR-M_* plane up to $z \sim 2$. *A&A*, 561:A86.

McMullin, J. P., Waters, B., Schiebel, D., Young, W., and Golap, K. (2007). CASA Architecture and Applications. In Shaw, R. A., Hill, F., and Bell, D. J., editors, *Astronomical Data Analysis Software and Systems XVI*, volume 376 of *Astronomical Society of the Pacific Conference Series*, page 127.

Michiyama, T., Saito, T., Tadaki, K.-i., Ueda, J., Zhuang, M.-Y., Molina, J., Lee, B., Wang, R., Bolatto, A. D., Iono, D., Nakanishi, K., Izumi, T., Yamashita, T., and Ho, L. C. (2021). An ACA Survey of [C I] $^3P_1$-$^3P_0$, CO J = 4 - 3, and Dust Continuum in Nearby U/LIRGs. *ApJS*, 257(2):28.

Narayanan, D., Krumholz, M. R., Ostriker, E. C., and Hernquist, L. (2012). A general model for the CO-H_2 conversion factor in galaxies with applications to the star formation law. *MNRAS*, 421(4):3127–3146.

Newman, S. F., Buschkamp, P., Genzel, R., Förster Schreiber, N. M., Kurk, J., Sternberg, A., Gnat, O., Rosario, D., Mancini, C., Lilly, S. J., Renzini, A., Burkert, A., Carollo, C. M., Cresci, G., Davies, R., Eisenhauer, F., Genel, S., Shapiro Griffin, K., Hicks, E. K. S., Lutz, D., Naab, T., Peng, Y., Tacconi, L. J., Wuyts, S., Zamorani, G., Vergani, D., and Weiner, B. J. (2014). Nebular Excitation in z ~2 Star-forming Galaxies from the SINS and LUCI Surveys: The Influence of Shocks and Active Galactic Nuclei. *ApJ*, 781(1):21.

Noeske, K. G., Weiner, B. J., Faber, S. M., Papovich, C., Koo, D. C., Somerville, R. S., Bundy, K., Conselice, C. J., Newman, J. A., Schiminovich, D., Le Floc'h, E., Coil, A. L., Rieke, G. H., Lotz, J. M., Primack, J. R., Barmby, P., Cooper, M. C., Davis, M., Ellis, R. S., Fazio, G. G., Guhathakurta, P., Huang, J., Kassin, S. A., Martin, D. C., Phillips, A. C., Rich, R. M., Small, T. A., Willmer, C. N. A., and Wilson, G. (2007). Star Formation in AEGIS Field Galaxies since z=1.1: The Dominance of Gradually Declining Star Formation, and the Main Sequence of Star-forming Galaxies. *ApJ*, 660(1):L43–L46.

Offner, S. S. R., Bisbas, T. G., Bell, T. A., and Viti, S. (2014). An alternative accurate tracer of molecular clouds: the 'XCi-factor'. *MNRAS*, 440:L81–L85.

Okada, Y., Güsten, R., Requena-Torres, M. A., Röllig, M., Stutzki, J., Graf, U. U., and Hughes, A. (2019). Velocity profiles of [C_{II}], [C_I], CO, and [O_I] and physical conditions in four star-forming regions in the Large Magellanic Cloud. *A&A*, 621:A62.

Papadopoulos, P. P. and Geach, J. E. (2012). Molecular and Atomic Line Surveys of Galaxies. II. Unbiased Estimates of their Star Formation Mode. *ApJ*, 757(2):157.

Papadopoulos, P. P., Thi, W. F., and Viti, S. (2004). CI lines as tracers of molecular gas, and their prospects at high redshifts. *MNRAS*, 351(1):147–160.

Pettini, M. and Pagel, B. E. J. (2004). [OIII]/[NII] as an abundance indicator at high redshift. *MNRAS*, 348(3):L59–L63.

Popping, G., Decarli, R., Man, A. W. S., Nelson, E. J., Béthermin, M., De Breuck, C., Mainieri, V., van Dokkum, P. G., Gullberg, B., van Kampen, E., Spaans, M., and Trager, S. C. (2017). ALMA reveals starburst-like interstellar medium conditions in a compact star-forming galaxy at z 2 using [CI] and CO. *A&A*, 602:A11.

Requena-Torres, M. A., Israel, F. P., Okada, Y., Güsten, R., Stutzki, J., Risacher, C., Simon, R., and Zinnecker, H. (2016). Carbon gas in SMC low-metallicity star-forming regions. *A&A*, 589:A28.

Rizzo, F., Roman-Oliveira, F., Fraternali, F., Frickmann, D., Valentino, F. M., Brammer, G., Zanella, A., Kokorev, V., Popping, G., Whitaker, K. E., Kohandel, M., Magdis, G. E., Di Mascolo, L., Ikeda, R., Jin, S., and Toft, S. (2023). The ALMA-ALPAKA survey. I. High-resolution CO and [CI] kinematics of star-forming galaxies at z = 0.5-3.5. *A&A*, 679:A129.

Rodighiero, G., Brusa, M., Daddi, E., Negrello, M., Mullaney, J. R., Delvecchio, I., Lutz, D., Renzini, A., Franceschini, A., Baronchelli, I., Pozzi, F., Gruppioni, C., Strazzullo, V., Cimatti, A., and Silverman, J. (2015). Relationship between Star Formation Rate and Black Hole Accretion At Z = 2: the Different Contributions in Quiescent, Normal, and Starburst Galaxies. *ApJ*, 800(1):L10.

Rodighiero, G., Daddi, E., Baronchelli, I., Cimatti, A., Renzini, A., Aussel, H., Popesso, P., Lutz, D., Andreani, P., Berta, S., Cava, A., Elbaz, D., Feltre, A., Fontana, A., Förster Schreiber, N. M., Franceschini, A., Genzel, R., Grazian, A., Gruppioni, C., Ilbert, O., Le Floch, E., Magdis, G., Magliocchetti, M., Magnelli, B., Maiolino, R., McCracken, H., Nordon, R., Poglitsch, A., Santini, P., Pozzi, F., Riguccini, L., Tacconi, L. J., Wuyts, S., and Zamorani, G. (2011). The Lesser Role of Starbursts in Star Formation at z = 2. *ApJ*, 739(2):L40.

Sandstrom, K. M., Leroy, A. K., Walter, F., Bolatto, A. D., Croxall, K. V., Draine, B. T., Wilson, C. D., Wolfire, M., Calzetti, D., Kennicutt, R. C., Aniano, G., Donovan Meyer, J., Usero, A., Bigiel, F., Brinks, E., de Blok, W. J. G., Crocker, A., Dale, D., Engelbracht, C. W., Galametz, M., Groves, B., Hunt, L. K., Koda, J., Kreckel, K., Linz, H., Meidt, S., Pellegrini, E., Rix, H. W., Roussel, H., Schinnerer, E., Schruba, A., Schuster, K. F., Skibba, R., van der Laan, T., Appleton, P., Armus, L., Brandl, B., Gordon, K., Hinz, J., Krause, O., Montiel, E., Sauvage, M., Schmiedeke, A., Smith, J. D. T., and Vigroux, L. (2013). The CO-to-H_2 Conversion Factor and Dust-to-gas Ratio on Kiloparsec Scales in Nearby Galaxies. *ApJ*, 777(1):5.

Schmidt, M. (1959). The Rate of Star Formation. *ApJ*, 129:243.

Schreiber, C., Elbaz, D., Pannella, M., Ciesla, L., Wang, T., and Franco, M. (2018). Dust temperature and mid-to-total infrared color distributions for star-forming galaxies at $0 < z < 4$. *A&A*, 609:A30.

Schruba, A., Leroy, A. K., Walter, F., Bigiel, F., Brinks, E., de Blok, W. J. G., Dumas, G., Kramer, C., Rosolowsky, E., Sandstrom, K., Schuster, K., Usero, A., Weiss, A., and Wiesemeyer, H. (2011). A Molecular Star Formation Law in the Atomic-gas-dominated Regime in Nearby Galaxies. *AJ*, 142(2):37.

Shimajiri, Y., Sakai, T., Tsukagoshi, T., Kitamura, Y., Momose, M., Saito, M., Oshima, T., Kohno, K., and Kawabe, R. (2013). Extensive [C I] Mapping toward the Orion-A Giant Molecular Cloud. *ApJ*, 774(2):L20.

Solomon, P. M. and Vanden Bout, P. A. (2005). Molecular Gas at High Redshift. *ARA&A*, 43(1):677–725.

Spilker, J. S., Aravena, M., Marrone, D. P., Béthermin, M., Bothwell, M. S., Carlstrom, J. E., Chapman, S. C., Collier, J. D., de Breuck, C., Fassnacht, C. D., Galvin, T., Gonzalez, A. H., González-López, J., Grieve, K., Hezaveh, Y., Ma, J., Malkan, M., O'Brien, A., Rotermund, K. M., Strandet, M., Vieira, J. D., Weiss, A., and Wong, G. F. (2015). Sub-kiloparsec Imaging of Cool Molecular Gas in Two Strongly Lensed Dusty, Star-forming Galaxies. *ApJ*, 811(2):124.

Spilker, J. S., Bezanson, R., Weiner, B. J., Whitaker, K. E., and Williams, C. C. (2019). Evidence for Inside-out Galaxy Growth and Quenching of a z ∼ 2 Compact Galaxy From High-resolution Molecular Gas Imaging. *ApJ*, 883(1):81.

Sun, J., Leroy, A. K., Ostriker, E. C., Meidt, S., Rosolowsky, E., Schinnerer, E., Wilson, C. D., Utomo, D., Belfiore, F., Blanc, G. A., Emsellem, E., Faesi, C., Groves, B., Hughes, A., Koch, E. W., Kreckel, K., Liu, D., Pan, H.-A., Pety, J., Querejeta, M., Razza, A., Saito, T., Sardone, A., Usero, A., Williams, T. G., Bigiel, F., Bolatto, A. D., Chevance, M., Dale, D. A., Gensior, J., Glover, S. C. O., Grasha, K., Henshaw, J. D., Jiménez-Donaire, M. J., Klessen, R. S., Kruijssen, J. M. D., Murphy, E. J., Neumann, L., Teng, Y.-H., and Thilker, D. A. (2023). Star Formation Laws and Efficiencies across 80 Nearby Galaxies. *ApJ*, 945(2):L19.

Tacchella, S., Carollo, C. M., Förster Schreiber, N. M., Renzini, A., Dekel, A., Genzel, R., Lang, P., Lilly, S. J., Mancini, C., Onodera, M., Tacconi, L. J., Wuyts, S., and Zamorani, G. (2018). Dust Attenuation, Bulge Formation, and Inside-out Quenching of Star Formation in Star-forming Main Sequence Galaxies at z ∼ 2. *ApJ*, 859(1):56.

Tacchella, S., Dekel, A., Carollo, C. M., Ceverino, D., DeGraf, C., Lapiner, S., Mandelker, N., and Primack, J. R. (2016). Evolution of density profiles in high-z galaxies: compaction and quenching inside-out. *MNRAS*, 458(1):242–263.

Tacchella, S., Lang, P., Carollo, C. M., Förster Schreiber, N. M., Renzini, A., Shapley, A. E., Wuyts, S., Cresci, G., Genzel, R., Lilly, S. J., Mancini, C., Newman, S. F., Tacconi, L. J., Zamorani, G., Davies, R. I., Kurk, J., and Pozzetti, L. (2015). SINS/zC-SINF Survey of z ∼ 2 Galaxy Kinematics: Rest-frame Morphology, Structure, and Colors from Near-infrared Hubble Space Telescope Imaging. *ApJ*, 802(2):101.

Tacconi, L. J., Genzel, R., Saintonge, A., Combes, F., García-Burillo, S., Neri, R., Bolatto, A., Contini, T., Förster Schreiber, N. M., Lilly, S., Lutz, D., Wuyts, S., Accurso, G., Boissier, J., Boone, F., Bouché, N., Bournaud, F., Burkert, A., Carollo, M., Cooper, M., Cox, P., Feruglio, C., Freundlich, J., Herrera-Camus, R., Juneau, S., Lippa, M., Naab, T., Renzini, A., Salome, P., Sternberg, A., Tadaki, K., Übler, H., Walter, F., Weiner, B., and Weiss, A. (2018). PHIBSS: Unified Scaling Relations of Gas Depletion Time and Molecular Gas Fractions. *ApJ*, 853(2):179.

Tacconi, L. J., Genzel, R., and Sternberg, A. (2020). The Evolution of the Star-Forming Interstellar Medium Across Cosmic Time. *ARA&A*, 58:157–203.

Tacconi, L. J., Neri, R., Genzel, R., Combes, F., Bolatto, A., Cooper, M. C., Wuyts, S., Bournaud, F., Burkert, A., Comerford, J., Cox, P., Davis, M., Förster Schreiber, N. M., García-Burillo, S., Gracia-Carpio, J., Lutz, D., Naab, T., Newman, S., Omont, A., Saintonge, A., Shapiro Griffin, K., Shapley, A., Sternberg, A., and Weiner, B. (2013). Phibss: Molecular Gas Content and

Scaling Relations in z ~1-3 Massive, Main-sequence Star-forming Galaxies. *ApJ*, 768(1):74.

Teague, R. and Foreman-Mackey, D. (2018). A Robust Method to Measure Centroids of Spectral Lines. *Research Notes of the American Astronomical Society*, 2(3):173.

Tielens, A. G. G. M. and Hollenbach, D. (1985). Photodissociation regions. II. A model for the Orion photodissociation region. *ApJ*, 291:747–754.

Valentino, F., Magdis, G. E., Daddi, E., Liu, D., Aravena, M., Bournaud, F., Cibinel, A., Cormier, D., Dickinson, M. E., Gao, Y., Jin, S., Juneau, S., Kartaltepe, J., Lee, M.-Y., Madden, S. C., Puglisi, A., Sanders, D., and Silverman, J. (2018). A Survey of Atomic Carbon [C I] in High-redshift Main-sequence Galaxies. *ApJ*, 869(1):27.

Valentino, F., Magdis, G. E., Daddi, E., Liu, D., Aravena, M., Bournaud, F., Cortzen, I., Gao, Y., Jin, S., Juneau, S., Kartaltepe, J. S., Kokorev, V., Lee, M.-Y., Madden, S. C., Narayanan, D., Popping, G., and Puglisi, A. (2020). The Properties of the Interstellar Medium of Galaxies across Time as Traced by the Neutral Atomic Carbon [C I]. *ApJ*, 890(1):24.

Villanueva, V., Bolatto, A., Vogel, S., Levy, R. C., Sánchez, S. F., Barrera-Ballesteros, J., Wong, T., Rosolowsky, E., Colombo, D., Rubio, M., Cao, Y., Kalinova, V., Leroy, A., Utomo, D., Herrera-Camus, R., Blitz, L., and Luo, Y. (2021). The EDGE-CALIFA Survey: The Resolved Star Formation Efficiency and Local Physical Conditions. *ApJ*, 923(1):60.

Villanueva, V., Bolatto, A. D., Vogel, S. N., Wong, T., Leroy, A. K., Sánchez, S. F., Levy, R. C., Rosolowsky, E., Colombo, D., Kalinova, V., Cronin, S., Teuben, P., Rubio, M., and Bazzi, Z. (2024). The EDGE-CALIFA Survey: Molecular Gas and Star Formation Activity across the Green Valley. *ApJ*, 962(1):88.

Walter, F., Carilli, C., Neeleman, M., Decarli, R., Popping, G., Somerville, R. S., Aravena, M., Bertoldi, F., Boogaard, L., Cox, P., da Cunha, E., Magnelli, B., Obreschkow, D., Riechers, D., Rix, H.-W., Smail, I., Weiss, A., Assef, R. J., Bauer, F., Bouwens, R., Contini, T., Cortes, P. C., Daddi, E., Diaz-Santos, T., González-López, J., Hennawi, J., Hodge, J. A., Inami, H., Ivison, R., Oesch, P., Sargent, M., van der Werf, P., Wagg, J., and Yung, L. Y. A. (2020). The Evolution of the Baryons Associated with Galaxies Averaged over Cosmic Time and Space. *ApJ*, 902(2):111.

Walter, F., Weiß, A., Downes, D., Decarli, R., and Henkel, C. (2011). A Survey of Atomic Carbon at High Redshift. *ApJ*, 730(1):18.

Weiß, A., Downes, D., Henkel, C., and Walter, F. (2005). Atomic carbon at redshift ∼2.5. *A&A*, 429:L25–L28.

Zolotov, A., Dekel, A., Mandelker, N., Tweed, D., Inoue, S., DeGraf, C., Ceverino, D., Primack, J. R., Barro, G., and Faber, S. M. (2015). Compaction and quenching of high-z galaxies in cosmological simulations: blue and red nuggets. *MNRAS*, 450(3):2327–2353.